HHS Public Access

Author manuscript

Cell Rep. Author manuscript; available in PMC 2022 July 18.

Published in final edited form as:

Cell Rep. 2022 July 05; 40(1): 111028. doi:10.1016/j.celrep.2022.111028.

Running speed and REM sleep control two distinct modes of rapid interhemispheric communication

Megha Ghosh[1,5], **Fang-Chi Yang**[1,5], **Sharena P. Rice**[1,2,5], **Vaughn Hetrick**[1], **Alcides Lorenzo Gonzalez**[1,2], **Danny Siu**[1], **Ellen K.W. Brennan**[1,2], **Tibin T. John**[1,2], **Allison M. Ahrens**[1], **Omar J. Ahmed**[1,2,3,4,6,*]

[1]Department of Psychology, University of Michigan, Ann Arbor, MI 48109, USA

[2]Neuroscience Graduate Program, University of Michigan, Ann Arbor, MI 48109, USA

[3]Kresge Hearing Research Institute, University of Michigan, Ann Arbor, MI 48109, USA

[4]Department of Biomedical Engineering, University of Michigan, Ann Arbor, MI 48109, USA

[5]These authors contributed equally

[6]Lead contact

SUMMARY

Rhythmic gamma-band communication within and across cortical hemispheres is critical for optimal perception, navigation, and memory. Here, using multisite recordings in both rats and mice, we show that even faster ~140 Hz rhythms are robustly anti-phase across cortical hemispheres, visually resembling splines, the interlocking teeth on mechanical gears. Splines are strongest in superficial granular retrosplenial cortex, a region important for spatial navigation and memory. Spline-frequency interhemispheric communication becomes more coherent and more precisely anti-phase at faster running speeds. Anti-phase splines also demarcate high-activity frames during REM sleep. While splines and associated neuronal spiking are anti-phase across retrosplenial hemispheres during navigation and REM sleep, gamma-rhythmic interhemispheric communication is precisely in-phase. Gamma and splines occur at distinct points of a theta cycle and thus highlight the ability of interhemispheric cortical communication to rapidly switch between in-phase (gamma) and anti-phase (spline) modes within individual theta cycles during both navigation and REM sleep.

Graphical Abstract

*Correspondence: ojahmed@umich.edu.

AUTHOR CONTRIBUTIONS

Conceptualization, O.J.A., M.G., F.-C.Y.; investigation, M.G., F.-C.Y., S.P.R., V.H., A.L.G., D.S., T.T.J., A.M.A., O.J.A.; software, M.G., D.S., T.T.J., O.J.A.; formal analysis, M.G., O.J.A.; visualization, M.G., S.P.R., E.K.W.B., O.J.A.; writing – original draft, M.G., O.J.A.; writing – review & editing, O.J.A., M.G., F.-C.Y., S.P.R., V.H., A.L.G., D.S., E.K.W.B., T.T.J., A.M.A.; funding acquisition & supervision, O.J.A.

SUPPLEMENTAL INFORMATION

Supplemental information can be found online at https://doi.org/10.1016/j.celrep.2022.111028.

DECLARATION OF INTERESTS

The authors declare no competing interests.

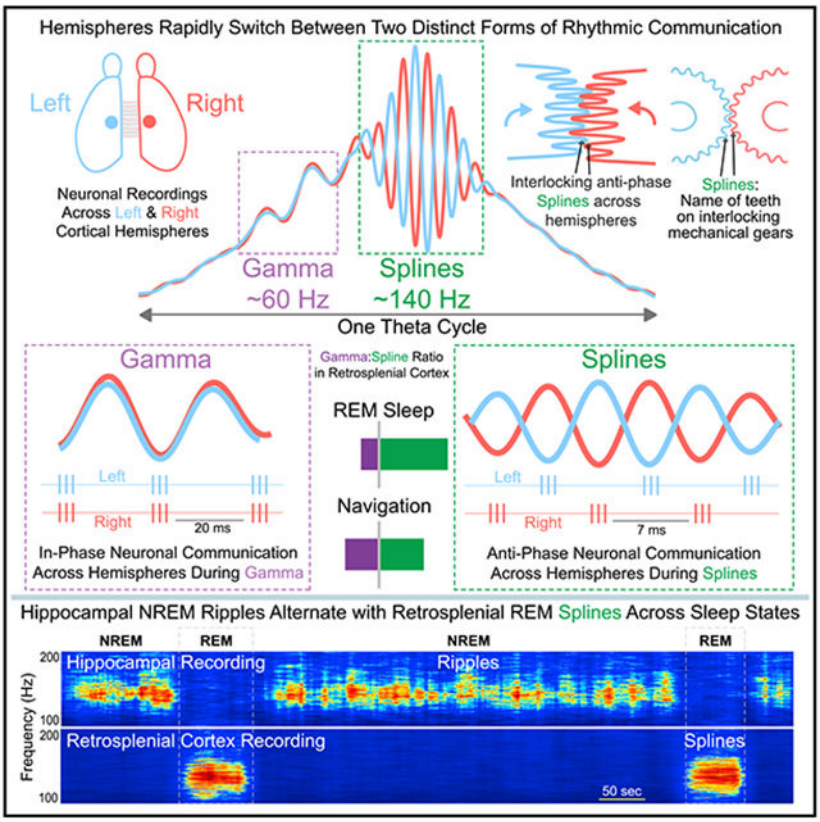

In brief

Gamma-rhythmic communication within and across cortical hemispheres is critical for optimal perception, navigation, and memory. Here, Ghosh et al. identify even faster ~140 Hz rhythms, named splines, that reflect anti-phase neuronal synchrony across hemispheres. The balance of anti-phase spline and in-phase gamma communication is dynamically controlled by behavior and sleep.

INTRODUCTION

Gamma-band oscillations are associated with a multitude of active behaviors, including navigation, sensory processing, and attention, as well as rapid eye movement (REM) sleep (Brosch and Budinger, 2002; Fries et al., 2001, 2008; Gray and Di Prisco, 1997; Gregoriou et al., 2009; Murthy and Fetz, 1996; Womelsdorf et al., 2006). These fast rhythms are relatively ubiquitous, having been observed across multiple species (humans [Chatrian et al., 1960]; monkeys [Murthy and Fetz, 1996]; cats [Gray et al., 1989]; turtles [Prechtl, 1994]; rodents [Buzsáki et al., 1983]; locusts [Laurent, 1996]) and brain regions (visual cortex [Gray et al., 1989]; sensorimotor cortices [Murthy and Fetz, 1992, 1996]; hippocampus [Bragin et al., 1995]; olfactory bulb [Freeman, 1978]). Gamma-rhythmic fluctuations seen in the extracellular local field potential (LFP) reflect the summed postsynaptic potentials (PSPs) onto multiple nearby neurons (Ahmed and Cash, 2013; Atallah and Scanziani, 2009; Kajikawa and Schroeder, 2011; Mitzdorf, 1985, 1991; Renshaw et al., 1940).

These PSPs can rhythmically synchronize the firing of neurons, helping to more robustly encode and transfer salient information (Ahmed and Cash, 2013; Colgin and Moser, 2010). Gamma-band synchrony with little to no phase lag is also seen among neurons separated by large distances, both within and across cortical regions (Colgin and Moser, 2010; Fries et al., 2008; Gray and Di Prisco, 1997; Gregoriou et al., 2009; Murthy and Fetz, 1996; Rodriguez et al., 1999; Roelfsema et al., 1997). This long-range gamma-band synchrony has been suggested to play a potentially important role in the temporal binding of concordant information (Engel et al., 2001; Tallon-Baudry and Bertrand, 1999) and also for the efficacious communication of information between coherent regions (Colgin and Moser, 2010; Fries et al., 2008; Womelsdorf et al., 2006). Similar in-phase coherence is seen at gamma-band frequencies across cortical hemispheres, helping to synchronize interhemispheric processing of related information (Bland et al., 2020; Cho et al., 2020; Engel et al., 1991).

Successful spatial navigation also involves precisely coordinated gamma-band communication between key circuits (Zheng et al., 2016). Hippocampal-entorhinal synaptic interactions, for example, are coherently coordinated at gamma-rhythmic frequencies during navigation (Colgin et al., 2009). This communication can show frequency-specific coupling across regions, with slow gamma frequencies synchronizing CA1-CA3 activity and faster gamma frequencies synchronizing CA1-entorhinal activity, and each of these rhythmic interactions is in-phase, regardless of the precise gamma frequency (Colgin et al., 2009; Zheng et al., 2016). Thus, as in the visual system (Engel et al., 1991; Gray et al., 1989), in-phase synchronization at gamma frequencies plays an important role in supporting communication between navigationally important brain regions.

The retrosplenial cortex (RSC) is also important for spatial navigation, with lesions leading to impaired memory and spatial disorientation in both humans and rodents (Alexander and Nitz, 2017; Alexander et al., 2020; Bottini et al., 1990; Czajkowski et al., 2014; Epstein, 2008; Hattori et al., 2019; Ino et al., 2007; Maguire, 2001; Takahashi et al., 1997; Vann et al., 2003, 2009). The RSC is interconnected with the hippocampal formation, visual cortex, posterior parietal cortex, contralateral RSC, and a number of subcortical structures, including the anterior thalamus (Brennan et al., 2021; van Groen and Wyss, 1992; van Groen et al., 1993; Kaitz and Robertson, 1981; Makino and Komiyama, 2015; Olsen et al., 2017; Shibata, 1993; Sripanidkulchai and Wyss, 1987; Vogt and Miller, 1983; Wilber et al., 2015; Yamawaki et al., 2019a, 2019b). Despite its importance, how the RSC coherently communicates with these other brain regions to carry out its navigational functions remains poorly understood. Recent work has identified 110–160 Hz oscillations in the RSC during both navigation and REM sleep (Alexander et al., 2018; Koike et al., 2017). Similar observations of ~110–160 Hz oscillations, though relatively rare, have been made in other brain regions (González et al., 2020; Scheffzük et al., 2011; Sirota et al., 2008; Tort et al., 2013). These rhythms have so far been referred to as either “high-frequency oscillations” (González et al., 2020; Scheffzük et al., 2011; Tort et al., 2013) or “fast gamma” (Alexander et al., 2018; Koike et al., 2017), reflecting their ambiguous nature and emphasizing the need to identify the regions whose neuronal ensembles communicate at this rhythmic frequency.

Here, using large-scale recordings in both rats and mice, we study the RSC as well as multiple related regions (hippocampus, visual cortex, posterior parietal cortex), and show that theta-coupled 110–160 Hz oscillations are strongest in the superficial layers of the granular retrosplenial cortex (RSG). We discover that these fast oscillations are the signature of anti-phase communication across hemispheres. This anti-phase coupling is robust during both REM sleep and movement and becomes even more precise at faster running speeds. These anti-phase 110–160 Hz oscillations across hemispheres resemble splines, the interlocking teeth on mechanical gears. For this reason, we henceforth refer to them as splines. Gamma oscillations, coupled to a distinct theta phase, are also seen in the RSG during navigation and are also coherent across hemispheres, but this communication is robustly in-phase. Our findings highlight two distinct channels of rapid interhemispheric communication during REM sleep and navigation, with gamma being in-phase and splines anti-phase. Thus, anti-phase splines and in-phase gamma are likely to support two computationally distinct communication channels, both implemented within individual theta cycles across a range of distinct behaviors and REM sleep.

RESULTS

Retrosplenial REM splines alternate with hippocampal non-REM ripples across sleep states

To compare fast oscillatory activity across hippocampal CA1, RSC, posterior parietal cortex (PPC), and visual cortex (V1), we first used custom microdrives and silicon probes to record multisite sleep-wake signals in rats (Figures S1 and 1A-1E). While typical non-REM (NREM) ripples (110–190 Hz) were found in hippocampal CA1, the most prominent fast oscillation observed in the cortex during sleep was a 110–160 Hz oscillation in the RSC during REM sleep (Figure 1C). For reasons outlined in the introduction and later in the results, we call these oscillations “splines.” Splines during REM sleep were strongest in the RSC (Figures 1B, 1D, and 1E). Retrosplenial REM splines consistently alternated with hippocampal NREM ripples across sleep states (Figures 1F-1H).

Population-averaged power spectra revealed clearly elevated spline (110–160 Hz) power during REM sleep selectively in the RSC (Figures 1I-1L; RSC: nine rats, 62 sessions, 257 channels; CA1: six rats, 58 sessions, 203 channels; PPC: two rats, 13 sessions, 16 channels; V1: three rats, 40 sessions, 93 channels). Normalized spline power during REM sleep was significantly higher in the RSC than in any other brain region examined (rank-sum test, $p < 0.0001$ in all cases; Figure 1M). On the other hand, normalized ripple power during NREM sleep was significantly higher in CA1 than all other brain regions (rank-sum test, $p < 0.05$ in all cases; Figure 1N). Similar results were obtained whether the data were normalized by broadband power (1–230 Hz; Figures 1M and 1N) or by theta power (5–11 Hz; data not shown). Thus, hippocampal ripples are the dominant fast oscillation during NREM sleep, but retrosplenial splines are the dominant fast network rhythm across the sampled brain regions during REM sleep, suggesting that the RSC is ideally suited to the study of splines. For this reason, we more heavily sampled the RSC compared with other cortical recording locations in this study.

Splines are precisely coupled to the peak of theta, most strongly in the granular retrosplenial cortex

Since theta and spline power co-occurred in the RSC during REM sleep (Figure 1), we next explored the temporal relationship between spline and theta rhythms to confirm and extend previous observations showing the presence of theta-coupled slow and fast gamma rhythms in the retrosplenial cortex (Alexander et al., 2018; Koike et al., 2017). Simultaneously recorded raw LFP traces from CA1, RSC, PPC, and V1 showed that splines selectively occur at the peak of RSC theta (Figures 2A-2C). Figure 2B shows representative theta cycles from three rats with splines consistently at the peak of each theta cycle. To study the strength of this phase-amplitude coupling of splines to the peak of theta, we used wavelet-based spectrograms and computed the strength of each fast frequency across the phases of theta cycles. Phase-amplitude plots across rats during REM (Figure 2C) confirmed that splines are strongest in RSC and precisely coupled to the peak of theta. To quantify the strength of coupling of splines to theta, we used the modulation index metric (Tort et al., 2010) and found it to be significantly higher in RSC compared with all other brain regions examined here (RSC: nine rats, 54 sessions, 216 channels; CA1: six rats, 50 sessions, 175 channels; PPC: two rats, nine sessions, 12 channels; V1: three rats, 35 sessions, 81 channels; rank-sum test, $p < 0.0001$).

Both REM and active awake states are associated with the appearance of theta rhythms. Consistently, we observed theta-coupled splines during freely moving behaviors. As during REM, awake splines were strongest in the RSC (Figures S2A and S2B) and were strongly coupled to the peak of theta (Figures S2C and S2D).

Since the RSC is subdivided into the dorsal dysgranular and ventral granular subdivisions (van Groen and Wyss, 1992, 2003; Domesick, 1968), we asked whether the coupling of splines to theta differed between these regions. We found that across these two subdivisions of the RSC, the strength of theta phase-amplitude coupling of splines increased with depth and was far stronger in the granular RSC than in the dysgranular RSC (Figure S3).

We next asked if the probability of spline occurrence was dependent on the amplitude of theta cycles. Despite the strong modulation of spline amplitude by the phase of the theta cycle in which splines occur, spline probability was not strongly controlled by theta amplitude and splines occurred in both high- and low-amplitude theta cycles (Figure S4A). Overall, theta amplitude and spline power were only weakly correlated (Figure S4B, median rho = 0.2, 9 rats, 54 sessions). Thus, the occurrence of prominent theta oscillations does not necessarily predict the occurrence of splines. However, when splines do occur, they are precisely coupled to the peak of the containing theta cycle.

Splines are associated with high-activity REM frames

We next aimed to understand the temporal patterning of spline occurrence during REM sleep and their correlation with the activity of retrosplenial and hippocampal single units. We classified cells into fast-spiking putative inhibitory neurons (FS) and regular-spiking putative excitatory neurons (RS) using their characteristic waveform shapes (Figure 3A). We quantified their mean firing rate during awake, NREM, and REM sleep states (Figure 3B).

Statistical comparisons were then run using repeated measures ANOVA followed by post hoc Tukey honest significant difference (HSD) tests. In CA1, FS cells fired more during REM sleep than during awake ($p < 0.001$) and NREM ($p < 0.001$) states. There was no significant difference in the firing rate of RS cells across brain states in CA1. In RSC, FS cells fired more during REM sleep than during awake ($p = 0.02$) and NREM ($p < 0.001$). RSC RS cells fired more during REM sleep compared with NREM ($p < 0.001$) with no significant difference in the firing rate between REM and awake ($p = 0.08$).

Next, using an objective algorithm to identify theta cycles with and without splines, we found that spline-containing theta cycles tended to occur in clusters within each REM epoch (Figure 3C). To confirm the presence of such spline-rich REM frames, we computed the probability of observing splines in a theta cycle, triggered off theta cycles with splines versus theta cycles without splines. The triggering cycle in this analysis is referred to as theta cycle 0. We found that when splines occurred in theta cycle 0, the probability of observing splines in adjacent theta cycles was elevated for up to ±22 adjacent theta cycles (Figure 3D; effect size ≥ 0.5). Thus, during REM sleep, splines occurred in clusters spanning multiple contiguous theta cycles.

To better understand the single unit correlates of splines, we asked if FS and RS cells had increased activity during spline compared with non-spline epochs. We found that the firing rate of both RSC and CA1 FS cells increased during spline-rich REM frames (Figures 3E and 3F). To quantify this observation, we computed the cycle-by-cycle firing rate of each cell during each REM theta cycle. We then compared this cycle-by-cycle firing rate triggered off theta cycles with splines versus theta cycles without splines (Figure 3G). The triggering cycle in this analysis is again referred to as theta cycle 0. The firing rate of FS cells was significantly higher (paired t test, $p < 0.01$) in theta cycles with splines (RSC: Mean = 15.98 Hz; CA1: Mean = 22.81 Hz) than in those without splines (RSC: Mean = 13.04 Hz; CA1: Mean = 15.8 Hz). Similarly, the firing rate of RS cells was also significantly higher (paired t test, $p < 0.01$) in theta cycles with splines (RSC: Mean = 11.95 Hz; CA1: Mean = 8.45 Hz) than in those without splines (RSC: Mean = 9.95 Hz; CA1: Mean = 4.41 Hz). We further found that when splines occurred in theta cycle 0, the firing rate of both RSC and CA1 FS cells was elevated for at least ±10 cycles (effect size ≥0.5), while RS rates were elevated for at least ±10 cycles (effect size ≥0.5) in RSC and −4 to +10 cycles in CA1 (effect size ≥0.5). Thus, spline-rich REM frames are accompanied by increased FS and RS cell activity.

Splines are correlated across the long axis of the retrosplenial cortex but occur independently of gamma

We next sought to understand whether splines at a given retrosplenial location were correlated with splines across the long axis of the RSC (see Figure S1 for recording sites spanning the RSC long axis) and whether splines were at all correlated with gamma at the same location. We sorted each theta cycle first by spline power (Figure 4A, left) and then by gamma power (Figure 4A, right). Theta cycles without splines still had gamma oscillations, while theta cycles without gamma oscillations very often contained splines. We confirmed this observation across the population: during REM, splines and gamma were very weakly correlated (rho = 0.22 across nine rats and 54 local electrodes; Figure 4B, middle). Similarly,

RSC splines were uncorrelated with gamma oscillations in CA1 (rho = 0.07 across six rats, 50 reference electrodes with 175 CA1 channels; Figure 4B; right). We then asked if splines were correlated across pairs of simultaneously recorded RSC signals and found that they were robustly correlated (rho = 0.7 across nine rats, 54 reference electrodes with 162 non-local RSC electrodes; Figure 4B, left). Similar observations were made during freely moving behavior (Figure 4C). Splines were significantly correlated across RSC (rho = 0.7) with weak correlations to local gamma (rho = 0.24; similar to observations by Alexander et al., 2018) and no correlation to CA1 gamma (rho = 0.15). Indeed, across the population, the correlation of splines across distant pairs of electrodes within the RSC was significantly higher than the correlation of splines with local gamma rhythms (rank-sum test, $p < 0.001$) or with CA1 gamma rhythms (rank-sum test, $p < 0.001$) during both REM and freely moving behavior. We next asked if spline and gamma duration varied with theta frequency. We found that while both spline and gamma event duration (i.e., how long a bout of spline or gamma cycles lasts within a theta cycle) decreased with increasing theta frequency (Figures S5A and S5C), single cycle duration was independent of theta frequency (Figures S5B and S5D). Thus, individual spline and gamma cycles remain distinct from each other at all theta frequencies.

Together these results show that splines are distinct from gamma and most often occur independently of gamma. Instead, splines co-occur across the long axis of the RSC.

Splines are also seen in mice

Are splines evolutionarily conserved across species? All data presented so far were recorded in rats, so we next recorded from mice with probes implanted in the RSC and CA1 during sleep and freely moving states. We found robust splines in mice (Figures S6B-S6D) that were strongest in the RSC, as seen in rats. Splines were strongly coupled to the peak of theta (Figure S6E), as in rats. In rats, spline-theta coupling was stronger in REM compared with awake states, while gamma-theta coupling was stronger during awake states compared with REM (Figures 4D and 4F). The exact same relationship was seen in mice (Figures 4E and 4G). Importantly, across all four conditions (rat REM and awake, mouse REM and awake), RSC splines were consistently more strongly coupled to theta than gamma. Thus, the quantitative properties of splines and gamma are remarkably well conserved across both rats and mice, making both species well suited to the study of splines.

Splines are strongest in the superficial layers of the granular retrosplenial cortex

While splines are highly correlated across the granular RSC (Figure 4B), is their strength uniform across layers or do they have a laminar power gradient? To more precisely understand the laminar correlates of splines, we implanted mice with silicon probes spanning both RSC hemispheres (Figure 5A). Figure 5B shows raw traces from all 32 simultaneously recorded channels (100 μm spacing) during an REM sleep epoch. Splines were evident in both left and right RSC (Figure 5B) and strongest in the superficial layers during both REM sleep and freely moving active states (Figures 5C and 5D), decreasing in amplitude as distance from the midline increased. Gamma oscillations were also strongest in the superficial layers. Current source density (CSD) analysis confirmed this observation showing the presence of strong sinks and sources in the superficial layers during both splines

(Figures S7A and S7B) and gamma (Figures S7C and S7D). Quantification of this effect showed that there was a significant effect of distance from midline on spline and gamma power during REM (spline power: $F(3,78) = 78.2$, $p < 0.0001$; gamma power: $F(3,78) = 26$, $p < 0.0001$) and freely moving states (spline power: $F(3,78) = 73.8$, $p < 0.0001$; gamma power: $F(3,78) = 31.7$, $p < 0.0001$). Post hoc Tukey HSD test indicated that mean spline power during REM and awake states significantly decreased with distance from midline ($p < 0.0001$). Similarly, gamma power for the group closest to midline was also significantly higher than those farther from the midline ($p < 0.0001$).

Splines are anti-phase across hemispheres while gamma oscillations are in-phase during both REM sleep and awake active states

Our probe recordings shown above reveal that splines and gamma are strongest in the superficial layers of RSG. We next examined the coherence between these oscillations across hemispheres. Simultaneously recorded raw LFP traces from superficial layers of the left and right hemisphere (Figure 6A) showed that splines were robustly and surprisingly anti-phase (180° out of phase) across hemispheres. On the contrary, gamma oscillations in the left and right hemispheres were in-phase. To further understand the phase relationship of splines and gamma across hemispheres, we utilized both time-domain and spectral coherence methods to robustly quantify this effect, and make sure that both types of analyses could confirm the visual observations. We computed cross-correlations between superficial channels in the left and right hemispheres from three mice (Figures 6B and 6C show individual examples). Splines were consistently anti-phase across hemispheres during both REM sleep and freely moving states. To quantify this phase relationship, we computed wavelet-based coherence between superficial channels from the left and right hemisphere during REM sleep and freely moving sessions. We then analyzed the distribution of coherence phase offset for splines and gamma during both brain states (Figures 6D and 6E). Population coherence magnitude and phase distribution (Figures 6F and 6G) from three mice (nine REM and nine freely moving sessions) showed that splines were selectively 180° out of phase across hemispheres. Gamma oscillations, on the other hand, were consistently in-phase. A Watson Williams test showed that there was a significant difference ($p < 0.0001$) between mean spline phase and gamma phase across hemispheres. Thus splines, and not gamma rhythms, are the signature of anti-phase coherence across hemispheres. Further, this phase relationship was seen in both tonic and phasic REM (Figure S8). This anti-phase property makes “splines” an apt name for these rhythms, named after mechanical splines—the similarly anti-phase interlocking teeth on mechanical gears (Figure S9).

We reasoned that anti-phase communication in the spline frequency band should result in phase locking of RSC neurons to opposite phases of spline oscillations across hemispheres. We classified single units using the same metrics used for the rat data (Figure 3) and found that all 20 units recorded in mice were putative RS cells (Figure S10A). Similar to RS cells in rats (Figure 3), these units showed lower firing rates during NREM sleep (Figure S10B) and increased firing during REM frames (Figures S10C and S10D). Figure 6H shows an example phase-locking distribution of a single unit recorded from superficial RSC, revealing a clear preference to fire at the trough of local ipsilateral splines and the peak of contralateral splines. Of the 20 single units recorded during REM and active states from the superficial

layers, 18 were significantly phase-locked to the trough of ipsilateral splines and 10 to the peak of contralateral splines (Figures 6I, S11A, and S11B). Similarly, all 19 multi-units recorded were significantly phase-locked to the trough of ipsilateral splines, and 18 to the peak of contralateral splines (Figures 6I, S11C, and S11D). Similar analysis for gamma showed significant phase-locking of cells to the trough of both ipsilateral and contralateral gamma (Figures 6J, 6K, and S11E-S11H). Indeed, while there was a significant difference between preferred spike phases for ipsilateral versus contralateral spline oscillations (Watson Williams test, $p < 0.0001$ for both single unit and multi-unit), there was no significant difference between preferred spike phases for ipsilateral versus contralateral gamma (Watson Williams text, $p = 0.16$ for single units, $p = 0.25$ for multi-units).

Running speed controls two distinct bands of interhemispheric communication

We next investigated how both anti-phase spline coupling and in-phase gamma coupling change with running speed. We used head-fixed mice running on a spherical ball to precisely control and track running speed. Phase-amplitude coupling of splines to theta in the superficial layers of RSG in a given hemisphere increased with running speed, with similar relationships seen for theta-gamma coupling (Figures 7A and 7E). A repeated measures ANOVA revealed a significant effect of speed on the modulation index of splines ($F(4,32) = 41.8$, $p < 0.001$) and gamma ($F(4,32) = 15.4$; $p < 0.001$). The effect size of increase in modulation index at the fastest speeds to that at the slowest running speeds was higher for splines ($d = 2.1$) as compared with gamma ($d = 1.4$). We next asked if interhemispheric coherence was also similarly modulated by running speed. To do so, we first aimed to understand how spline interhemispheric coherence changed within a theta cycle. Similar to theta phase-amplitude coupling (seen in a single hemisphere), we found that the magnitude of spline-spline interhemispheric coherence within a theta cycle was highest at the peak of theta (Figure 7B). Gamma-gamma interhemispheric coherence was highest at the rising phase of theta at all running speeds sampled. Consistently, splines were strongly anti-phase near the peak of theta, but coherence in this same 110–160 Hz frequency range was highly variable at other theta phases, where splines are rarely seen (Figures 7C and 7D). Next, to assess change in interhemispheric coherence with speed, we analyzed the coherence magnitude and the interhemispheric spline-spline or gamma-gamma phase offsets at various speeds. We found a significant effect of speed on the magnitude of spline ($F(4,32) = 30$, $p < 0.001$) and gamma coherence ($F(4,32) = 27$, $p < 0.001$). The effect size for the increase in coherence at the fastest speeds compared with the slowest running speeds was stronger for splines ($d = 1.2$) as compared with gamma ($d = 0.6$) (Figure 7F). Spline interhemispheric communication remained consistently anti-phase at all running speeds, while gamma remained in-phase (Figure 7G). Importantly, the precision of the interhemispheric communication increased with increasing running speed (Figure 7H). To quantify this, we analyzed the circular spread in the mean phase across a theta cycle using the mean resultant vector (R). There was a significant effect of speed on the mean resultant vector (R) for the phase offset for splines ($F(4,32) = 6$, $p < 0.001$) and gamma ($F(4,32) = 18.9$, $p < 0.001$). Similar to coherence magnitude, the effect size at faster speeds compared with slower speeds was stronger for splines ($d = 1.4$) as compared with gamma ($d = 0.4$). These results were not affected by theta frequency (Figure S12). Thus, running speed increases spline-spline interhemispheric

communication by making this coupling stronger and more precisely anti-phase. Gamma-gamma interhemispheric communication also becomes stronger and more precisely in-phase at faster running speeds. However, changes in spline-band interhemispheric communication are more pronounced than changes in gamma-band interhemispheric communication. These results show that the two distinct speed-controlled bands of anti-phase (splines) and in-phase (gamma) interhemispheric communication can co-exist, with the timing of each form of interhemispheric communication controlled by the phase of theta.

DISCUSSION

Interhemispheric communication can rapidly switch between in-phase and anti-phase modes within a single theta cycle

Gamma rhythms are arguably the best understood of the fast oscillations seen in the healthy mammalian brain during behavior. Both slow and fast gamma rhythms have been shown to support phase-related communication, often manifesting as in-phase LFP-LFP synchronization across brain regions (Colgin et al., 2009; Hsiao et al., 2016). Here, we show that faster ~140 Hz rhythms in the retrosplenial cortex (Alexander et al., 2018; Koike et al., 2017) are instead the signature of robust anti-phase communication across cortical hemispheres during both navigation and REM sleep (Figure 6). These rhythms visually resemble splines: the anti-phase, interlocking teeth on mechanical gears (Figure S9). Splines are strongest in the superficial layers of the RSG. RSG gamma rhythms are also strongest in the superficial layers but are consistently in-phase across RSG hemispheres. RSG splines and gamma occur during distinct phases of theta. This reveals a striking and underappreciated feature of interregional neuronal communication: two brain regions (left and right RSG in this case) can communicate using both in-phase and anti-phase rhythmic coherence, rapidly switching between the two modes within and across individual theta cycles (Figures 6 and 7).

The properties of hippocampal gamma rhythms within a single hemisphere are known to be controlled by running speed (Ahmed and Mehta, 2012; Gereke et al., 2018; Kemere et al., 2013; Sheeran and Ahmed, 2020; Zheng et al., 2015). Our results show that interhemispheric RSG coherence in both the gamma and spline bands increases with running speed in head-fixed mice, with a stronger effect on splines (Figure 7). Gamma rhythms become more precisely in-phase across RSG hemispheres at faster speeds while splines become more precisely anti-phase, with the effect size again being larger for splines (Figure 7). Our gamma results are in agreement with recent studies focused on distinct behaviors showing that interhemispheric gamma coherence is more strongly in-phase during more demanding and more successfully executed tasks (Bland et al., 2020; Cho et al., 2020). In contrast, our finding of increased interhemispheric spline coherence at faster speeds shows that more strongly activated brain states (such as running faster; Sheeran and Ahmed, 2020), can also improve and sharpen anti-phase communication across hemispheres. Thus, both in-phase gamma and anti-phase spline coherence can be altered by changes in running speed (Figure 7). It is also known that theta frequency increases, on average, with running speed (Ahmed and Mehta, 2012; Ghosh et al., 2020; Hinman et al., 2011; Scaplen et al., 2017; Sheeran and Ahmed, 2020; Sławińska and Kasicki, 1998; Whishaw and Vanderwolf,

1973), although there is considerable cycle-by-cycle variation in the properties of even consecutive theta cycles (Ghosh et al., 2020; Lopes-dos-Santos et al., 2018; Quinn et al., 2021). This means multiple theta frequency cycles are typically sampled at each speed. Our results show that regardless of the precise theta frequency sampled, splines remain anti-phase and continue to get more precise with increasing running speed (Figure S12). Furthermore, the duration of individual spline and gamma cycles is independent of theta frequency (Figure S5), showing that at all theta frequencies sampled, spline and gamma remain separate, independent rhythmic frequencies. Thus, anti-phase splines and in-phase gamma can represent distinct computational functions during individual theta cycles that have a range of theta frequencies and behavioral correlates (e.g., different running speeds and different REM sleep phases). The precise nature of these distinct computations and the relative advantages versus disadvantages of in-phase gamma versus anti-phase spline synchronization remain to be elucidated.

The defining features of splines and their possible mechanisms

Splines are characterized by four key defining features. First, splines are precisely phase-locked to the peak of local retrosplenial theta rhythms. Second, the spline frequency of 110–160 Hz is faster than the ranges traditionally attributed to either slow or fast gamma rhythms (Colgin et al., 2009). Third, splines are independent of gamma, but can co-occur in the same theta cycle as gamma. Fourth, splines are the signature of anti-phase communication across retrosplenial hemispheres, even though gamma rhythms (including those occurring in the same theta cycle) represent in-phase synchronization across hemispheres.

One of the standard models of gamma generation is the pyramidal-interneuron-gamma (PING) model, where excitatory neurons drive local FS inhibitory neurons that in turn provide feedback inhibition onto excitatory neurons (Börgers and Kopell, 2003; Tiesinga and Sejnowski, 2009; Traub et al., 1996). There are also theories that propose that FS-FS inhibition is chiefly responsible for the generation of gamma (interneuron-gamma [ING]; Cardin et al., 2009; Wang and Buzsáki, 1996; White et al., 1998; Whittington et al., 2000), although these theories are more likely to apply to faster gamma rhythms (Haufler and Pare, 2014; Jackson et al., 2011; Mann and Mody, 2010; Tort et al., 2013). Similar FS-FS inhibition models have been proposed to lead to the fast (~180 Hz) oscillations associated with hippocampal ripples (Schlingloff et al., 2014). Together, these previous models implicate FS-FS interactions in the generation of faster rhythms such as splines in the RSG. Indeed, we have found that RSG FS cells fire more during spline-rich frames (Figure 3). In the superficial layers of RSG, we have previously shown strong FS-FS connectivity (Brennan et al., 2020), indicative of a superficial RSG circuit well suited to the generation of splines via FS-FS interactions. Neurons ideally positioned to carry this spline frequency information to the contralateral RSG are also present in these same layers. Low Rheobase (LR) neurons, a uniquely small and hyperexcitable pyramidal cell localized to the superficial layers of the RSG, do not synapse locally (Brennan et al., 2020), instead sending their axons to the contralateral RSG via the corpus callosum (Brennan et al., 2020, 2021; van Groen and Wyss, 2003; Kurotani et al., 2013; Sripanidkulchai and Wyss, 1987). It is possible that these LR neurons may be able to directly couple left and right RSG, although the in-phase versus anti-phase implications of this connectivity remain to be determined.

Implications for neural coding during REM sleep and motivated behaviors

The retrosplenial cortex has been shown to be involved in not just spatial navigation and memory, but also fear conditioning and planning for (or imagining) the future (Alexander and Nitz, 2017; Alexander et al., 2020; Chang et al., 2020; Hinman et al., 2018; Kwapis et al., 2015; Mao et al., 2018; Miller et al., 2019, 2021). One of the anatomic connections thought to support this multitude of functions is the bidirectional connectivity of the RSC with the anterior thalamic nuclei (Aggleton et al., 2014; Brennan et al., 2021; Clark et al., 2010; van Groen et al., 1993; Jenkins et al., 2004; Vantomme et al., 2020; Wright et al., 2010; Yamawaki et al., 2019a), where a large proportion of cells encode head direction (HD) (Blair and Sharp, 1995; Clark and Taube, 2012; Tsanov et al., 2011). There have been reports of ~140 Hz cross-correlations between these thalamic HD cells (Butler and Taube, 2017; Peyrache et al., 2015), but the source of this synchronization remains unexplained. This suggests the hypothesis that splines generated in the RSG are propagated back to the anterior thalamus via corticothalamic projections, potentially explaining the 140 Hz cross-correlations observed among thalamic HD cells and helping to synchronize thalamic activity at spline frequency. However, a similar argument could be made for the RSG gamma oscillations observed during behavior. Thus, an important next step in understanding retrosplenial-thalamic circuit interactions will be to decipher the rules governing spline- versus gamma-band communication between the RSG and thalamus.

Several key behavioral dimensions (attention, motivation, navigation, and memory, for example) influence gamma rhythms and theta-gamma coupling (Alexander et al., 2018; Canolty et al., 2006; Fries et al., 2001; Köster et al., 2014; Womelsdorf et al., 2006). Thus, it is also likely that these factors will alter the precise balance between spline-band versus gamma-band communication. Indeed, we find distinct ratios of spline-to-gamma theta-coupling in REM sleep versus awake behaviors, with the spline-to-gamma ratio being higher during REM sleep compared with awake states (Figure 4). These ratios are likely to be influenced by the amount of external input coming into the RSG at each point in time, and distinct input sources (Brennan et al., 2021; van Groen and Wyss, 1990, 2003; Shibata and Naito, 2008; Sugar et al., 2011) may be better suited to preferentially control splines versus gamma. Thus, the study of this ratio across a range of additional behavioral conditions will be instrumental in deciphering the respective roles of in-phase gamma and anti-phase splines in behaviorally relevant neuronal computations. Importantly, the relative ratios of splines-to-gamma seen in different brain states is very similar across both mice and rats (Figure 4), suggesting that these ratios may reflect evolutionarily conserved computational functions. The strength of splines during REM sleep also suggests that they may be related to some of the computational functions attributed to REM sleep, perhaps including either strengthening or pruning of synapses (Calais et al., 2015; Rasch and Born, 2013; Silva et al., 2004; Zhou et al., 2020). Across hemispheres, anti-phase splines would lead to a 3- to 4-ms spike-timing differential between contralateral RSG ensembles. This timing would allow for relatively precise potentiation or depression of synapses implementing spike-timing-dependent-plasticity rules, helping to sculpt the information encoded by neurons across retrosplenial hemispheres (Brzosko et al., 2019; Dan and Poo, 2004).

The retrosplenial cortex shows altered activity in persons with depression (Ho et al., 1996), post-traumatic stress disorder (Fridman et al., 2017), and Alzheimer's disease (Nestor et al., 2003). Interhemispheric communication is also impaired in each of these disorders (Guo et al., 2013; Lakmache et al., 1998; Saar-Ashkenazy et al., 2016; Wang et al., 2015). Here, we have shown that splines are the rhythmic signature of precise anti-phase communication across retrosplenial hemispheres. Thus, we anticipate altered interhemispheric RSG-RSG communication during sleep and/or motivated behaviors in each of these clinical conditions. This suggests that a careful analysis of splines may also have the potential to serve as a biomarker for precisely diagnosing the severity of interhemispheric communication impairments in multiple disorders.

Limitations of the study

Our study has some limitations: in the mouse recordings, all of the sampled retrosplenial cells happened to be RS cells in the left hemisphere (although the recordings in rats sampled large numbers of both RS and FS cells). Thus, future work will confirm that the relationship seen between FS cells and splines in rats (Figure 3) is also seen in mice. Given the almost identical findings with RS cells in both mice and rats, it is likely that retrosplenial FS cell properties in relation to sleep states and splines will be similar to those seen in rats.

STAR★METHODS

RESOURCE AVAILABILITY

Lead contact—Further information and requests for resources should be directed to and will be fulfilled by the lead contact, Dr. Omar J. Ahmed (ojahmed@umich.edu).

Materials availability—This study did not generate new unique reagents.

Data and code availability—All data reported in this paper will be shared by the lead contact upon reasonable request. This paper does not report original code. Any additional information required to reanalyze the data reported in this paper is available from the lead contact upon request.

EXPERIMENTAL MODEL AND SUBJECT DETAILS

Subjects

Rats: Subjects were nine male rats 3–7 months of age (seven Long-Evans (Charles Rivers Laboratories; LE 006) and two Sprague Dawley rats (Charles Rivers Laboratories; SD 400)). Rats were socially housed before surgery and then singly housed in a temperature- and humidity-regulated colony maintained on a 12:12 h light:dark cycle. Experiments were carried out in the dark phase for the Long-Evans and during the light phase for the Sprague Dawley rats.

Mice: Subjects were three male C57BL/6 mice 4–5 months of age (The Jackson Laboratory; 000664). Mice were socially housed before surgery and then singly housed in a temperature- and humidity-regulated colony maintained on a 12:12 h light:dark cycle. Experiments spanned both the light and dark phases.

All procedures followed the NIH guidelines and were approved by the Institutional Animal Care and Use Committee of the University of Michigan.

METHOD DETAILS

Surgery—Animals were handled and habituated in the recording room for at least 3 days before surgery. Animals were prepared for surgery via isoflurane induction and atropine administration (subcutaneous, 0.05 mg/kg) and then maintained on a surgical anesthetic plane with 1–2.5% isoflurane for the duration of the procedure. Rats were implanted with custom microdrives (n = 6) or silicon probes (n = 3, two of which were made by Cambridge NeuroTech, UK and one made by NeuroNexus Technologies, USA). Skull screws were implanted at the midline-cerebellum, contralateral posterior parietal cortex, frontal cortex, and/or posterior-lateral cerebellum with the chosen reference usually midline-cerebellum. EMG leads were placed into the neck muscle of rats (stainless steel; AM Systems). Mice were implanted with custom titanium ring headposts (MIC583; H.E. Parmer Company; Nashville TN) and silicon probes (NeuroNexus Technologies, USA). Skull screws were implanted in posterior-lateral cerebellum. All implants were performed using a stereotaxic apparatus (Stoelting Co, Wood Dale, IL) and Picospritzer III (Parker Hannifin; Hollis, NH) with a 1.0 mm OD glass pipette.

Implant locations—Rat implantations targeted hippocampus (AP range: −4.16 to −4.8 mm; ML range: −2.8 to +3.3 mm), retrosplenial cortex (AP range: −3.2 to −6.5 mm; ML range: −2.5 to +1.6 mm, 0–45° medial/lateral angle), posterior parietal cortex (AP range: −4.16 to −4.35 mm; ML range: +2.6 to +3.5 mm), and visual cortex (AP range: −4.56 to −5.2 mm; ML range: +3 to +4.4 mm). All DVs were adjusted to position tetrodes in each of the target areas. Microdrives were fabricated in-house using tetrodes made of four twisted nichrome wires with 1/4 hard pack insulation (RO800 alloy; Sandivik – Kanthal, Palm Coast, FL). Figure S1 shows the recording locations for each tetrode and probe in the rats.

Mouse implantations targeted bilateral retrosplenial cortex and unilateral subiculum/CA1 hippocampus (AP −2.30 mm; ML range −1.6 to +1.2 mm on a 55° angle; with the driven axis spanning superficial to deep RSC, across the midline, through contralateral RSG, corpus callosum, and into subiculum/CA1).

All electrophysiological recordings for both rats and mice started after 3 to 5 days of recovery from surgery.

Electrophysiological recordings

Rat recordings: Electrophysiological signals for all Long-Evans rats were acquired continuously and digitized at 32 kHz on a 64-channel Digital Lynx SX acquisition system with Cheetah recording and acquisition software (Neuralynx, Inc, MT). Single-unit activity was bandpass filtered between 600 Hz-6 kHz, and local field potentials were bandpass filtered between 0.1 Hz-8 kHz. The final signals were stored with timestamps and position information for subsequent analysis. Electrophysiological signals for the Sprague Dawley rats were amplified, filtered (0.1 Hz–8 kHz), and digitized at 30 kHz on the head stage

(RHD 2132, Intan Technologies Inc, CA) then passed to an Open Ephys acquisition system (Siegle et al., 2017). For recording sleep-wake states, rats were placed in a 36 cm diameter octagon turntable and allowed to sleep or move freely for up to 6 hours.

Mouse recordings: Electrophysiological signals were acquired using an Open Ephys system as described above. Recordings were performed during three behaviors. For sleep-wake states, mice were placed in a 31.75 cm by 31.75 cm by 28 cm tall square box, and allowed to sleep or move freely for up to 10 hours. For controlled running speed, the mice were head-fixed onto a freely rotating, light-weight, EPS foam sphere of 17 cm diameter with an optical rotary encoder (Bourns ENS1J-B28-L00256L-ND) to measure running speed. These sessions lasted 30 to 60 minutes. For self-generated navigational, two of the three mice were placed in a T-maze to explore freely for 30 minutes, while the third mouse was placed in a two-dimensional box similar to the one used for sleep-wake states. The T-maze had a long arm of 76.2 cm divided by a central arm of 30.5 cm length. Walls were 10 cm high and uniform in color and pattern for all arms.

Histology—After the last recording session, animals were deeply anesthetized with isoflurane, and the final recording site was marked with an electrolytic lesion (~20 μA for 10 seconds). Animals were then perfused with 1x PBS, followed by 4% paraformaldehyde. The brains were post-fixed for 24 hours in 4% paraformaldehyde and then transferred to a 30% sucrose solution until the time for sectioning. The brains were sectioned at a thickness of 40 μm and stained for Nissl material.

Single unit analysis—Spikes associated with putative individual units were isolated offline based on waveform characteristics and using a variety of partially automated and manual techniques (Offline Sorter, Plexon, Inc.). Spike waveforms of isolated units were then used for classifying the sorted units into FS and RS cells. Absolute ratio of the trough to peak amplitude of the spike waveform and the width of the spike waveform at 25% of the amplitude from the peak (P25Width) were used for an automated clustering via a Gaussian mixture model (Figure 3A). The posterior probability of the clusters identified boundary values of the amplitude ratio and P25Width, and we thereafter defined FS cells as those having a P25Width < 0.38 and absolute trough to peak amplitude < 1.5. This classification thus identified 333 RS and 63 FS cells in CA1, 295 RS and 48 FS cells in RSC and 38 RS and 5 FS cells in V1 in the data recorded from rats and 20 RSC RS cells in the mice data-set.

Movement analysis—Green and red LEDs on the headstages were used to track rats. Position tracking for the freely-moving and T-Maze set-ups was performed using DeepLabCut (Mathis et al., 2018). Extracted positions (x,y) were up-sampled to a 100 Hz and smoothed with a 1 Hz low-pass filter before computing speed as $\sqrt{\frac{dx^2}{dt} + \frac{dy^2}{dt}}$. Running speed for the head-fixed set-up was computed using the displacement of an optical rotary encoder attached to the spherical ball.

LFP analysis

Spectral analysis: The raw LFP was down-sampled to a 1,000 Hz. LFP power spectral analysis for classifying brain states and assessing brain-state specific oscillations (Figure 1) was performed using multi taper analysis with a window size of 5 seconds, time-bandwidth product of 1, and a taper of 1 using the chronux toolbox (https://chronux.org/). Spectral whitening was performed to equalize the variance across frequencies and adjust for the 1/f decrease in power with frequency that leads to overemphasis of lower frequencies. A second order autoregressive model (A) was used to model the raw LFP, and then a filter of [1;-A] was applied to normalize power across frequencies. To obtain the whitened spectrum, the same multi taper analysis mentioned above was performed on this filtered LFP. While plotting spectra in Figure 1, 60 Hz noise and its third harmonic were removed by setting power in a 1 Hz range of 59.5–60.5 Hz and 179.5–180.5 Hz as NaNs and interpolating power in these 1 Hz ranges based on the power values in the nearest frequency bins.

Brain state classification: Brain state was classified into awake, rapid eye movement (REM) sleep, non-REM (NREM) sleep, and unclassified (UnCS) using a semi-automated algorithm. EMG was filtered in the 0.5–100 Hz range. Thereafter, a root mean square value of the filtered EMG (rmsEMG) was computed using moving windows of 1 s with an overlap of 0.5 s. Movement speed was averaged using 1 s moving windows with an overlap of 0.5 s. High rmsEMG (> 0.25) and high speed (> 1 cm/s) were used to identify awake epochs. High delta (0.5–4 Hz) power (greater than the median z-scored power), low EMG, and lack of movement were used to identify NREM. Two NREM epochs separated by less than 3s were combined together as one. A NREM epoch of less than 4 seconds was discarded. Theta ratio was computed as the ratio of theta (5–11 Hz) power to a sum of delta and alpha (12–30 Hz) powers (theta/(delta+alpha)). An epoch with high theta ratio, detected by a threshold of 0.5+median z-scored theta ratio, accompanied with low EMG and speed, was classified as REM. NREM and REM epochs lasting less than 4s were not analyzed. Time epochs which did not meet any of the above criteria were labeled as unclassified. All classifications were manually verified. Ambiguous epochs were labeled as unclassified. The resulting final hypnogram had a resolution of 0.5 s.

Normalized spline and ripple power: To obtain a normalized value of power in the 110–160 Hz (spline) and ripple (110–190 Hz) frequency ranges during REM and NREM sleep, respectively, we used the ratio of power in the respective high frequency band to broadband (1–230 Hz) power both prior to and after spectral whitening.

Theta phase-amplitude coupling: Morlet wavelet spectrogram for each channel was computed for the entire session. It was z-scored to normalize every frequency across the session while comparing phase-amplitude coupling across brain regions (Figure 2C). Morlet windows were defined as described previously (Tallon-Baudry et al., 1997). A wavelet family of 7 was chosen. To get the Morlet spectrogram, the signal was convolved with the wavelets. To compute the theta phase coupling across frequencies, individual theta cycles were detected by filtering in the 6–12 Hz range. Thereafter, every time point in the theta cycle was converted to phase by linear transformation such that the start (trough) of a theta cycle was 0°, peak was 180°, and the end (next trough) was 360°. Power across frequencies

in a theta cycle was obtained from the wavelet spectrogram values in the corresponding theta cycle over 20-degree bins. Phase-amplitude coupling for a session during REM or awake was computed by averaging across theta cycles in the corresponding brain state.

Modulation index: Strength of the phase-amplitude coupling was quantified using modulation index as defined previously (Tort et al., 2010). Power in the spline band (110–160 Hz) or gamma band (30–80 Hz) over 20-degree bins across a theta cycle was obtained from the phase-amplitude matrix computed above. This power was normalized by the sum of power in the respective frequency range across all 360 degrees of the theta cycles, and its distance from a uniform distribution was computed using the following formula:

$$MI = \frac{\sum_{i=1}^{N} A(i) \times \log\left(\frac{A(i)}{U(i)}\right)}{\log(N)}$$

where A is normalized spine amplitude for the respective bins, U is the uniform distribution, and N is the total number of bins. The resulting measure, known as the modulation index (MI), quantifies the extent of phase-amplitude coupling between the two oscillations.

Kappa: We also computed the concentration parameter, kappa, of the von Mises distribution to quantify the strength of theta phase-amplitude coupling using the CircStat toolbox for MATLAB (Berens, 2009).

Detecting splines within theta cycles: Using the wavelet spectrogram, each theta cycle had an associated spectrum. Theta cycles were thereafter sorted by power in the 110–160 Hz range. Change point analysis was used to detect theta cycles with splines.

Spline-single unit firing rate analysis: Correlations between spline power and firing rate were computed over 25 ms bins.

Firing rate in individual theta cycles was computed by dividing the number of spikes in each theta cycle by the duration of the cycle.

Coherence analysis: Wavelet spectrograms as described above were used to compute coherence magnitude and phase for the entire REM or awake session. 10 ms smoothing windows were used. Thereafter, mean spline and gamma coherence magnitude and phase were computed over individual theta cycles. For analyzing modulation of coherence by theta phase, mean coherence magnitude and phase offset were computed over 20-degree bins. All awake analysis was performed for linear speeds >5 cm/s.

Spike phase locking: Spline cycles were extracted by filtering the LFP in the 110–160 Hz range and finding local troughs and peaks. Spikes were assigned a phase with the starting trough as 0, peak as 180, and end of the cycle as 360°. For spike phase locking to gamma, the LFP was filtered in the 30–80 Hz range to identify local troughs and peaks and phase assignment of spikes was performed as for splines. Note that multi-units in Figures 6, S10, and S11 contain spike times from multiple units, while single-units have spike times from a single sorted unit.

Spline correlations across brain regions: To correlate power in various frequency bands across tetrodes in a given session, theta cycles with peaks closest to those of a reference tetrode in RSC were found. Thereafter, spline (110–160 Hz) power in those matched theta cycles was correlated across other simultaneously recorded RSC tetrodes, which we refer to as non-local RSC spline correlation (Figure 4). Spline-gamma correlations for RSC were computed by correlating spline power to gamma (30–80 Hz) power in theta cycles from the same reference tetrode (local gamma, Figure 4). Spline-gamma correlation with respect to CA1 was performed by correlating spline power in the RSC reference tetrode to gamma power in matched theta cycles from simultaneously recorded CA1 channels. To compute correlation between theta amplitude and spline power, we defined theta amplitude of a single-cycle as the difference between the z-scored amplitude values of the peak and starting trough.

Computing spline and gamma duration: Individual spline cycles were detected by filtering in the 110–160 Hz range and gamma cycles by filtering in the 30–80 Hz range. A spline or gamma event within a theta cycle was defined as the duration during which the amplitude of the filtered trace in each band was at least half of the peak value within that theta cycle. To ensure accurate detection, only theta cycles >3z in amplitude with peak spline or gamma amplitude greater than their median amplitude were chosen.

Current source density (CSD): LFP was centered 20 ms around peak spline amplitude in each theta cycle for spline CSD and 40 ms around peak gamma amplitude in each theta cycle for gamma CSD during REM sleep, freely moving or head-fixed running. These spline and gamma triggered LFPs were then averaged across 3 mice for each brain state. CSD was computed for this averaged LFP using the standard method (2B-A-C for 3 consecutive channels) similar to Montgomery et al. (2009).

Phasic REM detection: Phasic REM was detected similar to previous studies (Hammer et al., 2021; Mizuseki et al., 2011). Potential phasic REM epochs were identified as those where theta duration was below the 20th percentile of the theta cycles. Thereafter, only epochs having a duration of at least 1 second with mean theta amplitude greater than the mean amplitude across entire REM were identified as phasic REM.

Head-fixed speed analysis: To assess modulation of coherence by running speed, five speed categories were chosen: 0–0.5, 0.5–3, 3–8, 8–18, and 18–38 cm/s. These speed bins were chosen to represent the full range of running speeds, keeping the number of theta cycles in each bin nearly the same. Each theta cycle was assigned a speed value by computing speed at the peak of a theta cycle. Thereafter, theta cycles corresponding to each speed category were chosen, and phase-amplitude coupling, as mentioned above, was obtained for those theta cycles. Each theta cycle was assigned the peak coherence in that cycle. Coherence phase corresponding to the peak coherence magnitude was then assigned to each theta cycle. Thereafter, averaging over theta cycles for each speed bin was performed. The mean resultant vector (CircStat toolbox) of the distribution of mean coherence phase was computed for every speed bin.

QUANTIFICATION AND STATISTICAL ANALYSIS

A Wilcoxon rank sum test was used to compare power in spline and ripple bands and the strength of phase-amplitude coupling of splines across brain regions. A significant deviation from normality was confirmed using the Shapiro-Wilk test before using rank sum tests. To compare the correlation of splines across pairs of simultaneously recorded RSC signals with those recorded from CA1, we used a rank sum test. Repeated measures ANOVA followed by Tukey HSD test was used to compare firing rates between brain states. Only sessions with all 3 brain states were considered. Cohen's d value of 0.5 was chosen to compare firing rates centered at theta cycles with splines to those centered at theta cycles without spline to include medium and high effect size. A paired t-test was used to compare firing rates in theta cycles with and without splines. To compare the strength of splines and gamma oscillations across layers, channels were grouped based on their distance from the midline channel with each group spanning 300 μm. Normalization was performed by power in the midline channel for the respective band. A repeated measures ANOVA, followed by a Tukey HSD test was used to quantify the effect. The CircStat toolbox for MATLAB (Berens, 2009) was used for computing kappa, calculating the mean resultant vector and performing Watson Williams test for comparing mean spline coherence phase distributions of ipsilateral and contralateral channels. The mean resultant vector (R) is a measure of the spread of angular data. To compute R, each angle is transformed into a unit vector with slope β. R is obtained by a vector average across all of these unit vectors. If the angular data has a uniform distribution, R would be 0 and if all angles are equal then R would be 1. Hence, a higher value of R for the phase-offset across hemispheres would denote a higher precision of the phase-offset. Rayleigh's Z (CircStat toolbox) was used to test the significance of phase locking of units to splines from both local and contralateral channels. A repeated measures ANOVA was used to test the effect of speed on coherence magnitude and modulation index. Cohen's d was used to quantify effect size between the fastest (18–38 cm/s) speed and slowest (0.5–3 cm/s) speed bins. 0.5–3 cm/s was chosen as the reference for comparing effect of running speed instead of 0–0.5 cm/s since 0–0.5 cm/s included epochs of non-movement as well. Results were presented as mean ± standard error of the mean (SEM). An alpha value of 0.05 was used throughout.

Supplementary Material

Refer to Web version on PubMed Central for supplementary material.

ACKNOWLEDGMENTS

This work was supported by: startup funds from the University of Michigan (O.J.A.); NIH R21NS121745 (O.J.A.); NIH P50NS123067 (O.J.A.); Whitehall Foundation (O.J.A.); NIH T32-DC00011 (S.P.R.); NIH T32-NS076401 (S.P.R., A.L.G., E.K.W.B., T.T.J.); and NSF graduate fellowships (E.K.W.B., T.T.J.).

REFERENCES

Aggleton JP, Saunders RC, Wright NF, and Vann SD (2014). The origin of projections from the posterior cingulate and retrosplenial cortices to the anterior, medial dorsal and laterodorsal thalamic nuclei of macaque monkeys. Eur. J. Neurosci 39, 107–123. 10.1111/ejn.12389. [PubMed: 24134130]

Ahmed OJ, and Cash SS (2013). Finding synchrony in the desynchronized EEG: the history and interpretation of gamma rhythms. Front. Integr. Neurosci 7, 58. 10.3389/fnint.2013.00058. [PubMed: 23964210]

Ahmed OJ, and Mehta MR (2012). Running speed alters the frequency of hippocampal gamma oscillations. J. Neurosci 32, 7373–7383. 10.1523/jneurosci.5110-11.2012. [PubMed: 22623683]

Alexander AS, and Nitz DA (2017). Spatially periodic activation patterns of retrosplenial cortex encode route sub-spaces and distance traveled. Curr. Biol 27, 1551–1560.e4. 10.1016/j.cub.2017.04.036. [PubMed: 28528904]

Alexander AS, Rangel LM, Tingley D, and Nitz DA (2018). Neurophysiological signatures of temporal coordination between retrosplenial cortex and the hippocampal formation. Behav. Neurosci 132, 453–468. 10.1037/bne0000254. [PubMed: 30070554]

Alexander AS, Carstensen LC, Hinman JR, Raudies F, Chapman GW, and Hasselmo ME (2020). Egocentric boundary vector tuning of the retrosplenial cortex. Sci. Adv 6, eaaz2322. 10.1126/sciadv.aaz2322. [PubMed: 32128423]

Atallah BV, and Scanziani M (2009). Instantaneous modulation of gamma oscillation frequency by balancing excitation with inhibition. Neuron 62, 566–577. 10.1016/j.neuron.2009.04.027. [PubMed: 19477157]

Berens P (2009). CircStat : a MATLAB toolbox for circular statistics. J. Stat. Softw 31, 1–21. 10.18637/jss.v031.i10.

Blair HT, and Sharp PE (1995). Anticipatory head direction signals in anterior thalamus: evidence for a thalamocortical circuit that integrates angular head motion to compute head direction. J. Neurosci 15, 6260–6270. 10.1523/jneurosci.15-09-06260.1995. [PubMed: 7666208]

Bland NS, Mattingley JB, and Sale MV (2020). Gamma coherence mediates interhemispheric integration during multiple object tracking. J. Neurophysiol 123, 1630–1644. 10.1152/jn.00755.2019. [PubMed: 32186427]

Börgers C, and Kopell N (2003). Synchronization in networks of excitatory and inhibitory neurons with sparse, random connectivity. Neural Comput. 15, 509–538. 10.1162/089976603321192059. [PubMed: 12620157]

Bottini G, Cappa S, Geminiani G, and Sterzi R (1990). Topographic disorientation-A case report. Neuropsychologia 2, 521–540. 10.1093/neucas/2.6.521-f.

Bragin A, Jando G, Nádasdy Z, Hetke J, Wise K, and Buzsáki G (1995). Gamma (40-100 Hz) oscillation in the hippocampus of the behaving rat. J. Neurosci 15, 47–60. 10.1523/jneurosci.15-01-00047.1995. [PubMed: 7823151]

Brennan EKW, Sudhakar SK, Jedrasiak-Cape I, John TT, and Ahmed OJ (2020). Hyperexcitable neurons enable precise and persistent information encoding in the superficial retrosplenial cortex. Cell Rep. 30, 1598–1612.e8. 10.1016/j.celrep.2019.12.093. [PubMed: 32023472]

Brennan EKW, Jedrasiak-Cape I, Kailasa S, Rice SP, Sudhakar SK, and Ahmed OJ (2021). Thalamus and claustrum control parallel layer 1 circuits in retrosplenial cortex. Elife 10, e62207. 10.7554/elife.62207. [PubMed: 34170817]

Brosch M, and Budinger E (2002). Stimulus-related gamma oscillations in primate auditory cortex. J. Neurophysiol 87, 2715–2725. [PubMed: 12037173]

Brzosko Z, Mierau SB, and Paulsen O (2019). Neuromodulation of spike-timing-dependent plasticity: past, present, and future. Neuron 103, 563–581. 10.1016/j.neuron.2019.05.041. [PubMed: 31437453]

Butler WN, and Taube JS (2017). Oscillatory synchrony between head direction cells recorded bilaterally in the anterodorsal thalamic nuclei. J. Neurophysiol 117, 1847–1852. 10.1152/jn.00881.2016. [PubMed: 28250151]

Buzsáki G, Lai-Wo SL, and Vanderwolf CH (1983). Cellular bases of hippocampal EEG in the behaving rat. Brain Res. Rev 6, 139–171. 10.1016/0165-0173(83)90037-1.

Calais JB, Ojopi EB, Morya E, Sameshima K, and Ribeiro S (2015). Experience-dependent upregulation of multiple plasticity factors in the hippocampus during early REM sleep. Neurobiol. Learn. Mem 122, 19–27. 10.1016/j.nlm.2015.01.002. [PubMed: 25626078]

Canolty RT, Edwards E, Dalal SS, Soltani M, Nagarajan SS, Kirsch HE, Berger MS, Barbaro NM, and Knight RT (2006). High gamma power is phase-locked to theta oscillations in human neocortex. Science 313, 1626–1628. 10.1126/science.1128115. [PubMed: 16973878]

Cardin JA, Carlén M, Meletis K, Knoblich U, Zhang F, Deisseroth K, Tsai LH, and Moore CI (2009). Driving fast-spiking cells induces gamma rhythm and controls sensory responses. Nature 459, 663–667. 10.1038/nature08002. [PubMed: 19396156]

Chang HR, Esteves IM, Neumann AR, Sun J, Mohajerani MH, and McNaughton BL (2020). Coordinated activities of retrosplenial ensembles during resting-state encode spatial landmarks. Philos. Trans. R. Soc. B Biol. Sci 375, 20190228. 10.1098/rstb.2019.0228.

Chatrian GE, Bickford RG, and Uihlein A (1960). Depth electrographic study of a fast rhythm evoked from the human calcarine region by steady illumination. Electroencephalogr. Clin. Neurophysiol 12, 167–176. 10.1016/0013-4694(60)90070-5. [PubMed: 13809431]

Cho KKA, Davidson TJ, Bouvier G, Marshall JD, Schnitzer MJ, and Sohal VS (2020). Cross-hemispheric gamma synchrony between prefrontal parvalbumin interneurons supports behavioral adaptation during rule shift learning. Nat. Neurosci 23, 892–902. 10.1038/s41593-020-0647-1. [PubMed: 32451483]

Clark BJ, and Taube JS (2012). Vestibular and attractor network basis of the head direction cell signal in subcortical circuits. Front. Neural Circuits 6, 7. 10.3389/fncir.2012.00007. [PubMed: 22454618]

Clark BJ, Bassett JP, Wang SS, and Taube JS (2010). Impaired head direction cell representation in the anterodorsal thalamus after lesions of the retrosplenial cortex. J. Neurosci 30, 5289–5302. 10.1523/jneurosci.3380-09.2010. [PubMed: 20392951]

Colgin LL, and Moser EI (2010). Gamma oscillations in the hippocampus. Physiology 25, 319–329. 10.1152/physiol.00021.2010. [PubMed: 20940437]

Colgin LL, Denninger T, Fyhn M, Hafting T, Bonnevie T, Jensen O, Moser MB, and Moser EI (2009). Frequency of gamma oscillations routes flow of information in the hippocampus. Nature 462, 353–357. 10.1038/nature08573. [PubMed: 19924214]

Czajkowski R, Jayaprakash B, Wiltgen B, Rogerson T, Guzman-Karlsson MC, Barth AL,Trachtenberg JT, and Silva AJ (2014). Encoding and storage of spatial information in the retrosplenial cortex. Proc. Natl. Acad. Sci. U S A 111, 8661–8666. 10.1073/pnas.1313222111. [PubMed: 24912150]

Domesick VB (1968). Projections from the cingulate cortex in the rat. Brain Res. 12, 296–320. 10.1016/0006-8993(69)90002-x.

Dan Y, and Poo MM (2004). Spike timing-dependent plasticity of neural circuits. Neuron 44, 23–30. 10.1016/j.neuron.2004.09.007. [PubMed: 15450157]

Engel AK, König P, Kreiter AK, and Singer W (1991). Interhemispheric synchronization of oscillatory neuronal responses in cat visual cortex. Science 252, 1177–1179. 10.1126/science.252.5009.1177. [PubMed: 2031188]

Engel AK, Fries P, and Singer W (2001). Dynamic predictions: oscillations and synchrony in top–down processing. Nat. Rev. Neurosci 2, 704–716. 10.1038/35094565. [PubMed: 11584308]

Epstein RA (2008). Parahippocampal and retrosplenial contributions to human spatial navigation. Trends Cogn. Sci 12, 388–396. 10.1016/j.tics.2008.07.004. [PubMed: 18760955]

Freeman WJ (1978). Spatial properties of an EEG event in the olfactory bulb and cortex. Electroencephalogr. Clin. Neurophysiol 44, 586–605. 10.1016/0013-4694(78)90126-8. [PubMed: 77765]

Fridman A, Alkozei A, Smith R, Challener S, and Killgore WDS (2017). 575. Resiliency is associated with reduced activation within the retrosplenial cortex and secondary motor area for individuals with PTSD during anticipation of a negative event. Biol. Psychiatry 81, S232–S233. 10.1016/j.biopsych.2017.02.445.

Fries P, Reynolds JH, Rorie AE, and Desimone R (2001). Modulation of oscillatory neuronal synchronization by selective visual attention. Science 291, 1560–1563. 10.1126/science.1055465. [PubMed: 11222864]

Fries P,Womelsdorf T, Oostenveld R, and Desimone R (2008). The effects of visual stimulation and selective visual attention on rhythmic neuronal synchronization in macaque area V4. J. Neurosci 28, 4823–4835. 10.1523/jneurosci.4499-07.2008. [PubMed: 18448659]

Gereke BJ, Mably AJ, and Colgin LL (2018). Experience-dependent trends in CA1 theta and slow gamma rhythms in freely behaving mice. J. Neurophysiol 119, 476–489. 10.1152/jn.00472.2017. [PubMed: 29070630]

Ghosh M, Shanahan BE, Furtak SC, Mashour GA, Burwell RD, and Ahmed OJ (2020). Instantaneous amplitude and shape of postrhinal theta oscillations differentially encode running speed. Behav. Neurosci 134, 516–528. 10.1037/bne0000416. [PubMed: 33570992]

González J, Cavelli M, Mondino A, Rubido N, BL Tort A, and Torterolo P (2020). Communication through coherence by means of cross-frequency coupling. Neuroscience 449, 157–164. 10.1016/j.neuroscience.2020.09.019. [PubMed: 32926953]

Gray CM, and Viana Di Prisco G (1997). Stimulus-dependent neuronal oscillations and local synchronization in striate cortex of the alert cat. J. Neurosci 17, 3239–3253. 10.1523/jneurosci.17-09-03239.1997. [PubMed: 9096157]

Gray CM, König P, Engel AK, and Singer W (1989). Oscillatory responses in cat visual cortex exhibit inter-columnar synchronization which reflects global stimulus properties. Nature 338, 334–337. 10.1038/338334a0. [PubMed: 2922061]

Gregoriou GG, Gotts SJ, Zhou H, and Desimone R (2009). High-frequency, long-range coupling between prefrontal and visual cortex during attention. Science 324, 1207–1210. 10.1126/science.1171402. [PubMed: 19478185]

Guo W, Liu F, Dai Y, Jiang M, Zhang J, Yu L, Long L, Chen H, Gao Q, and Xiao C (2013). Decreased interhemispheric resting-state functional connectivity in first-episode, drug-naive major depressive disorder. Prog. Neuro Psychopharmacol. Biol. Psychiatry 41, 24–29. 10.1016/j.pnpbp.2012.11.003.

Hammer M, Schwale C, Brankačk J, Draguhn A, and Tort ABL (2021). Theta-gamma coupling during REM sleep depends on breathing rate. Sleep 44, zsab189. 10.1093/sleep/zsab189. [PubMed: 34297128]

Hattori R, Danskin B, Babic Z, Mlynaryk N, and Komiyama T (2019). Area-specificity and plasticity of history-dependent value coding during learning. Cell 177, 1858–1872.e15. 10.1016/j.cell.2019.04.027. [PubMed: 31080067]

Haufler D, and Pare D (2014). High-frequency oscillations are prominent in the extended amygdala. J. Neurophysiol 112, 110–119. 10.1152/jn.00107.2014. [PubMed: 24717353]

Hinman JR, Penley SC, Long LL, Escabí MA, and Chrobak JJ (2011). Septotemporal variation in dynamics of theta: speed and habituation. J. Neurophysiol 105, 2675–2686. 10.1152/jn.00837.2010. [PubMed: 21411562]

Hinman JR, Dannenberg H, Alexander AS, and Hasselmo ME (2018). Neural mechanisms of navigation involving interactions of cortical and subcortical structures. J. Neurophysiol 119, 2007–2029. 10.1152/jn.00498.2017. [PubMed: 29442559]

Ho AP, Gillin JC, Buchsbaum MS, Wu JC, Abel L, and Bunney WE (1996). Brain glucose metabolism during non-rapid eye movement sleep in major depression: a positron emission tomography study. Arch. Gen. Psychiatry 53, 645. 10.1001/archpsyc.1996.01830070095014. [PubMed: 8660131]

Hsiao Y-T, Zheng C, and Colgin LL (2016). Slow gamma rhythms in CA3 are entrained by slow gamma activity in the dentate gyrus. J. Neurophysiol 116, 2594–2603. 10.1152/jn.00499.2016. [PubMed: 27628206]

Ino T, Doi T, Hirose S, Kimura T, Ito J, and Fukuyama H (2007). Directional disorientation following left retrosplenial hemorrhage: a case report with fMRI studies. Cortex 43, 248–254. 10.1016/s0010-9452(08)70479-9. [PubMed: 17405670]

Jackson J, Goutagny R, and Williams S (2011). Fast and slow gamma rhythms are intrinsically and independently generated in the subiculum. J. Neurosci 31, 12104–12117. 10.1523/jneurosci.1370-11.2011. [PubMed: 21865453]

Jenkins TA,Vann SD, Amin E, and Aggleton JP (2004). Anterior thalamic lesions stop immediate early gene activation in selective laminae of the retrosplenial cortex: evidence of covert pathology in rats? Eur. J. Neurosci 19, 3291–3304. 10.1111/j.0953-816x.2004.03421.x. [PubMed: 15217385]

Kaitz SS, and Robertson RT (1981). Thalamic connections with limbic cortex. II. Corticothalamic projections. J. Comp. Neurol 195, 527–545. 10.1002/cne.901950309. [PubMed: 7204660]

Kajikawa Y, and Schroeder CE (2011). How local is the local field potential? Neuron 72, 847–858. 10.1016/j.neuron.2011.09.029. [PubMed: 22153379]

Kemere C, Carr MF, Karlsson MP, and Frank LM (2013). Rapid and continuous modulation of hippocampal network state during exploration of new places. PLoS One 8, e73114. 10.1371/journal.pone.0073114. [PubMed: 24023818]

Koike BDV, Farias KS, Billwiller F, Almeida-Filho D, Libourel PA, Tiran-Cappello A, Parmentier R, Blanco W, Ribeiro S, Luppi PH, and Queiroz CM (2017). Electrophysiological evidence that the retrosplenial cortex displays a strong and specific activation phased with hippocampal theta during paradoxical (REM) sleep. J. Neurosci 37, 8003–8013. 10.1523/jneurosci.0026-17.2017. [PubMed: 28729438]

Köster M, Friese U, Schöne B, Trujillo-Barreto N, and Gruber T (2014). Theta-gamma coupling during episodic retrieval in the human EEG. Brain Res. 1577, 57–68. 10.1016/j.brainres.2014.06.028. [PubMed: 24978601]

Kurotani T, Miyashita T, Wintzer M, Konishi T, Sakai K, Ichinohe N, and Rockland KS (2013). Pyramidal neurons in the superficial layers of rat retrosplenial cortex exhibit a late-spiking firing property. Brain Struct. Funct 218, 239–254. 10.1007/s00429-012-0398-1. [PubMed: 22383041]

Kwapis JL, Jarome TJ, Lee JL, and Helmstetter FJ (2015). The retrosplenial cortex is involved in the formation of memory for context and trace fear conditioning. Neurobiol. Learn. Mem 123, 110–116. 10.1016/j.nlm.2015.06.007. [PubMed: 26079095]

Lakmache Y, Lassonde M, Gauthier S, Frigon JY, and Lepore F (1998). Interhemispheric disconnection syndrome in Alzheimer's disease. Proc. Natl. Acad. Sci. U S A 95, 9042–9046. 10.1073/pnas.95.15.9042. [PubMed: 9671801]

Laurent G (1996). Dynamical representation of odors by oscillating and evolving neural assemblies. Trends Neurosci. 19, 489–496. 10.1016/s0166-2236(96)10054-0. [PubMed: 8931275]

Lopes-dos-Santos V, van de Ven GM, Morley A, Trouche S, Campo-Urriza N, and Dupret D (2018). Parsing hippocampal theta oscillations by nested spectral components during spatial exploration and memory-guided behavior. Neuron 100, 940–952.e7. 10.1016/j.neuron.2018.09.031. [PubMed: 30344040]

Maguire E (2001). The retrosplenial contribution to human navigation: a review of lesion and neuroimaging findings. Scand. J. Psychol 42, 225–238. 10.1111/1467-9450.00233. [PubMed: 11501737]

Makino H, and Komiyama T (2015). Learning enhances the relative impact of top-down processing in the visual cortex. Nat. Neurosci 18, 1116–1122. 10.1038/nn.4061. [PubMed: 26167904]

Mann EO, and Mody I (2010). Control of hippocampal gamma oscillation frequency by tonic inhibition and excitation of interneurons. Nat. Neurosci 13, 205–212. 10.1038/nn.2464. [PubMed: 20023655]

Mao D, Neumann AR, Sun J, Bonin V, Mohajerani MH, and McNaughton BL (2018). Hippocampus-dependent emergence of spatial sequence coding in retrosplenial cortex. Proc. Natl. Acad. Sci. U S A 115, 8015–8018. 10.1073/pnas.1803224115. [PubMed: 30012620]

Mathis A, Mamidanna P, Cury KM, Abe T, Murthy VN, Mathis MW, and Bethge M (2018). DeepLabCut: markerless pose estimation of user-defined body parts with deep learning. Nat. Neurosci 21, 1281–1289. 10.1038/s41593-018-0209-y. [PubMed: 30127430]

Miller AMP, Mau W, and Smith DM (2019). Retrosplenial cortical representations of space and future goal locations develop with learning. Curr. Biol 29, 2083–2090.e4. 10.1016/j.cub.2019.05.034. [PubMed: 31178316]

Miller AMP, Serrichio AC, and Smith DM (2021). Dual-factor representation of the environmental context in the retrosplenial cortex. Cereb. Cortex 31, 2720–2728. 10.1093/cercor/bhaa386. [PubMed: 33386396]

Mitzdorf U (1985). Current source-density method and application in cat cerebral cortex: investigation of evoked potentials and EEG phenomena. Physiol. Rev 65, 37–100. 10.1152/physrev.1985.65.1.37. [PubMed: 3880898]

Mitzdorf U (1991). Physiological sources of evoked potentials. Electroencephalogr. Clin. Neurophysiol Suppl. 42, 47–57.

Mizuseki K, Diba K, Pastalkova E, and Buzsáki G (2011). Hippocampal CA1 pyramidal cells form functionally distinct sublayers. Nat. Neurosci 14, 1174–1181. 10.1038/nn.2894. [PubMed: 21822270]

Montgomery SM, Betancur MI, and Buzsáki G (2009). Behavior-dependent coordination of multiple theta dipoles in the hippocampus. J. Neurosci 29, 1381–1394. 10.1523/jneurosci.4339-08.2009. [PubMed: 19193885]

Murthy VN, and Fetz EE (1992). Coherent 25- to 35-Hz oscillations in the sensorimotor cortex of awake behaving monkeys. Proc. Natl. Acad. Sci. U S A 89, 5670–5674. 10.1073/pnas.89.12.5670. [PubMed: 1608977]

Murthy VN, and Fetz EE (1996). Oscillatory activity in sensorimotor cortex of awake monkeys: synchronization of local field potentials and relation to behavior. J. Neurophysiol 76, 3949–3967. 10.1152/jn.1996.76.6.3949. [PubMed: 8985892]

Nestor PJ, Fryer TD, Ikeda M, and Hodges JR (2003). Retrosplenial cortex (BA 29/30) hypometabolism in mild cognitive impairment (prodromal Alzheimer's disease). Eur. J. Neurosci 18, 2663–2667. 10.1046/j.1460-9568.2003.02999.x. [PubMed: 14622168]

Olsen GM, Ohara S, Iijima T, and Witter MP (2017). Parahippocampal and retrosplenial connections of rat posterior parietal cortex. Hippocampus 27, 335–358. 10.1002/hipo.22701. [PubMed: 28032674]

Peyrache A, Lacroix MM, Petersen PC, and Buzsáki G (2015). Internally organized mechanisms of the head direction sense. Nat. Neurosci 18, 569–575. 10.1038/nn.3968. [PubMed: 25730672]

Prechtl JC (1994). Visual motion induces synchronous oscillations in turtle visual cortex. Proc. Natl. Acad. Sci. U S A 91, 12467–12471. 10.1073/pnas.91.26.12467. [PubMed: 7809060]

Quinn AJ, Lopes-dos-Santos V, Huang N, Liang W-K, Juan C-H, Yeh J-R, Nobre AC, Dupret D, and Woolrich MW (2021). Within-cycle instantaneous frequency profiles report oscillatory waveform dynamics. J. Neurophysiol 126, 1190–1208. 10.1152/jn.00201.2021. [PubMed: 34406888]

Rasch B, and Born J (2013). About sleep's role in memory. Physiol. Rev 93, 681–766. 10.1152/physrev.00032.2012. [PubMed: 23589831]

Renshaw B, Forbes A, and Morison BR (1940). Activity of isocortex and hippocampus: electrical studies with micro-electrodes. J. Neurophysiol 3, 74–105. 10.1152/jn.1940.3.1.74.

Rodriguez E, George N, Lachaux JP, Martinerie J, Renault B, and Varela FJ (1999). Perception's shadow: long-distance synchronization of human brain activity. Nature 397, 430–433. 10.1038/17120. [PubMed: 9989408]

Roelfsema PR, Engel AK, König P, and Singer W (1997). Visuomotor integration is associated with zero time-lag synchronization among cortical areas. Nature 385, 157–161. 10.1038/385157a0. [PubMed: 8990118]

Saar-Ashkenazy R, Veksler R, Guez J, Jacob Y, Shelef I, Shalev H, Friedman A, and Cohen JE (2016). Breakdown of inter-hemispheric connectivity is associated with posttraumatic symptomatology and memory impairment. PLoS One 11, e0144766. 10.1371/journal.pone.0144766. [PubMed: 26863536]

Scaplen KM, Ramesh RN, Nadvar N, Ahmed OJ, and Burwell RD (2017). Inactivation of the lateral entorhinal area increases the influence of visual cues on hippocampal place cell activity. Front. Syst. Neurosci 11, 40. 10.3389/fnsys.2017.00040. [PubMed: 28611603]

Scheffzük C, Kukushka VI, Vyssotski AL, Draguhn A, Tort ABL, and Brankačk J (2011). Selective coupling between theta phase and neocortical fast gamma oscillations during REM-sleep in mice. PLoS One 6, e28489. 10.1371/journal.pone.0028489. [PubMed: 22163023]

Schlingloff D, Káli S, Freund TF, Hájos N, and Gulyás AI (2014). Mechanisms of sharp wave initiation and ripple generation. J. Neurosci 34, 11385–11398. 10.1523/jneurosci.0867-14.2014. [PubMed: 25143618]

Sheeran WM, and Ahmed OJ (2020). The neural circuitry supporting successful spatial navigation despite variable movement speeds. Neurosci. Biobehav. Rev 108, 821–833. 10.1016/j.neubiorev.2019.11.013. [PubMed: 31760048]

Shibata H (1993). Efferent projections from the anterior thalamic nuclei to the cingulate cortex in the rat. J. Comp. Neurol 330, 533–542. 10.1002/cne.903300409. [PubMed: 8320343]

Shibata H, and Naito J (2008). Organization of anterior cingulate and frontal cortical projections to the retrosplenial cortex in the rat. J. Comp. Neurol 506, 30–45. 10.1002/cne.21523. [PubMed: 17990270]

Siegle JH, López AC, Patel YA, Abramov K, Ohayon S, and Voigts J (2017). Open Ephys: an open-source, plugin-based platform for multichannel electrophysiology. J. Neural. Eng 14, 045003. 10.1088/1741-2552/aa5eea. [PubMed: 28169219]

Silva RH, Chehin AB, Kameda SR, Takatsu-Coleman AL, Abílio VC, Tufik S, and Frussa-Filho R (2004). Effects of pre- or post-training paradoxical sleep deprivation on two animal models of learning and memory in mice. Neurobiol. Learn. Mem 82, 90–98. 10.1016/j.nlm.2004.04.005. [PubMed: 15341794]

Sirota A, Montgomery S, Fujisawa S, Isomura Y, Zugaro M, and Buzsáki G (2008). Entrainment of neocortical neurons and gamma oscillations by the hippocampal theta rhythm. Neuron 60, 683–697. 10.1016/j.neuron.2008.09.014. [PubMed: 19038224]

Sławińska U, and Kasicki S (1998). The frequency of rat's hippocampal theta rhythm is related to the speed of locomotion. Brain Res. 796, 327–331. 10.1016/s0006-8993(98)00390-4. [PubMed: 9689489]

Sripanidkulchai K, and Wyss JM (1987). The laminar organization of efferent neuronal cell bodies in the retrosplenial granular cortex. Brain Res. 406, 255–269. 10.1016/0006-8993(87)90790-6. [PubMed: 2436715]

Sugar J, Witter MP, van Strien NM, and Cappaert NLM (2011). The retrosplenial cortex: intrinsic connectivity and connections with the (Para) Hippocampal region in the rat. An interactive connectome. Front. Neuroinform 5, 7. 10.3389/fninf.2011.00007. [PubMed: 21847380]

Takahashi N, Kawamura M, Shiota J, Kasahata N, and Hirayama K (1997). Pure topographic disorientation due to right retrosplenial lesion. Neurology 49, 464–469. 10.1212/wnl.49.2.464. [PubMed: 9270578]

Tallon-Baudry C, and Bertrand O (1999). Oscillatory gamma activity in humans and its role in object representation. Trends Cogn. Sci 3, 151–162. 10.1016/s1364-6613(99)01299-1. [PubMed: 10322469]

Tallon-Baudry C, Bertrand O, Delpuech C, and Pernier J (1997). Oscillatory γ-band (30-70 Hz) activity induced by a visual search task in humans. J. Neurosci 17, 722–734. 10.1523/jneurosci.17-02-00722.1997. [PubMed: 8987794]

Tiesinga P, and Sejnowski TJ (2009). Cortical enlightenment: are attentional gamma oscillations driven by ING or PING? Neuron 63, 727–732. 10.1016/j.neuron.2009.09.009. [PubMed: 19778503]

Tort ABL, Komorowski R, Eichenbaum H, and Kopell N (2010). Measuring phase-amplitude coupling between neuronal oscillations of different frequencies. J. Neurophysiol 104, 1195–1210. 10.1152/jn.00106.2010. [PubMed: 20463205]

Tort ABL, Scheffer-Teixeira R, Souza BC, Draguhn A, and Brankačk J (2013). Theta-associated high-frequency oscillations (110-160Hz) in the hippocampus and neocortex. Prog. Neurobiol 100, 1–14. 10.1016/j.pneurobio.2012.09.002. [PubMed: 23022096]

Traub RD, Whittington MA, Colling SB, Buzsáki G, and Jefferys JGR (1996). Analysis of gamma rhythms in the rat hippocampus in vitro and in vivo. J. Physiol 493, 471–484. 10.1113/jphysiol.1996.sp021397. [PubMed: 8782110]

Tsanov M, Chah E, Vann SD, Reilly RB, Erichsen JT, Aggleton JP, and O'Mara SM (2011). Theta-modulated head direction cells in the rat anterior thalamus. J. Neurosci 31, 9489–9502. 10.1523/jneurosci.0353-11.2011. [PubMed: 21715614]

Vann SD, Wilton LAK, Muir JL, and Aggleton JP (2003). Testing the importance of the caudal retrosplenial cortex for spatial memory in rats. Behav. Brain Res 140, 107–118. 10.1016/s0166-4328(02)00274-7. [PubMed: 12644284]

Vann SD, Aggleton JP, and Maguire EA (2009). What does the retrosplenial cortex do? Nat. Rev. Neurosci 10, 792–802. 10.1038/nrn2733. [PubMed: 19812579]

Vantomme G, Rovó Z, Cardis R, Béard E, Katsioudi G, Guadagno A, Perrenoud V, Fernandez LMJ, and Lüthi A (2020). A thalamic reticular circuit for head direction cell tuning and spatial navigation. Cell Rep. 31, 107747. 10.1016/j.celrep.2020.107747. [PubMed: 32521272]

van Groen T, and Wyss JM (1990). Connections of the retrosplenial granular a cortex in the rat. J. Comp. Neurol 300, 593–606. 10.1002/cne.903000412. [PubMed: 2273095]

van Groen T, and Wyss JM (1992). Connections of the retrosplenial dysgranular cortex in the rat. J. Comp. Neurol 315, 200–216. 10.1002/cne.903150207. [PubMed: 1545009]

van Groen T, and Wyss JM (2003). Connections of the retrosplenial granular b cortex in the rat. J. Comp. Neurol 463, 249–263. 10.1002/cne.10757. [PubMed: 12820159]

van Groen T, Vogt BA, and Wyss JM (1993). Interconnections between the thalamus and retrosplenial cortex in the rodent brain. In Neurobiology of Cingulate Cortex and Limbic Thalamus, Vogt. and Gabriel., eds. (Birkhäuser), pp. 123–150.

Vogt BA, and Miller MW (1983). Cortical connections between rat cingulate cortex and visual, motor, and postsubicular cortices. J. Comp. Neurol 216, 192–210. 10.1002/cne.902160207. [PubMed: 6863602]

Wang XJ, and Buzsáki G (1996). Gamma oscillation by synaptic inhibition in a hippocampal interneuronal network model. J. Neurosci 16, 6402–6413. 10.1523/jneurosci.16-20-06402.1996. [PubMed: 8815919]

Wang Z, Wang J, Zhang H, Mchugh R, Sun X, Li K, and Yang QX (2015). Interhemispheric functional and structural disconnection in Alzheimer's disease: a combined resting-state fMRI and DTI study. PLoS One 10, e0126310. 10.1371/journal.pone.0126310. [PubMed: 25938561]

Whishaw IQ, and Vanderwolf CH (1973). Hippocampal EEG and behavior: change in amplitude and frequency of RSA (Theta rhythm) associated with spontaneous and learned movement patterns in rats and cats. Behav. Biol 8, 461–484. 10.1016/s0091-6773(73)80041-0. [PubMed: 4350255]

White JA, Chow CC, Ritt J, Soto-Treviño C, and Kopell N (1998). Synchronization and oscillatory dynamics in heterogeneous, mutually inhibited neurons. J. Comput. Neurosci 5, 5–16. 10.1023/a:1008841325921. [PubMed: 9580271]

Whittington MA, Traub RD, Kopell N, Ermentrout B, and Buhl EH (2000). Inhibition-based rhythms: experimental and mathematical observations on network dynamics. Int. J. Psychophysiol 38, 315–336. [PubMed: 11102670]

Wilber AA, Clark BJ, Demecha AJ, Mesina L, Vos JM, and McNaughton BL (2015). Cortical connectivity maps reveal anatomically distinct areas in the parietal cortex of the rat. Front. Neural Circuits 8, 146. 10.3389/fncir.2014.00146. [PubMed: 25601828]

Womelsdorf T, Fries P, Mitra PP, and Desimone R (2006). Gamma-band synchronization in visual cortex predicts speed of change detection. Nature 439, 733–736. 10.1038/nature04258. [PubMed: 16372022]

Wright NF, Erichsen JT, Vann SD, O'Mara SM, and Aggleton JP (2010). Parallel but separate inputs from limbic cortices to the mammillary bodies and anterior thalamic nuclei in the rat. J. Comp. Neurol 518, 2334–2354. 10.1002/cne.22336. [PubMed: 20437531]

Yamawaki N, Li X, Lambot L, Ren LY, Radulovic J, and Shepherd GM (2019a). Long-range inhibitory intersection of a retrosplenial thalamocortical circuit by apical tuft-targeting CA1 neurons. Nat. Neurosci 22, 618–626. [PubMed: 30858601]

Yamawaki N, Corcoran KA, Guedea AL, Shepherd GMG, and Radulovic J (2019b). Differential contributions of glutamatergic Hippocampal→Retrosplenial cortical projections to the formation and persistence of context memories. Cereb. Cortex 29, 2728–2736. 10.1093/cercor/bhy142. [PubMed: 29878069]

Zheng C, Bieri KW, Trettel SG, and Colgin LL (2015). The relationship between gamma frequency and running speed differs for slow and fast gamma rhythms in freely behaving rats. Hippocampus 25, 924–938. 10.1002/hipo.22415. [PubMed: 25601003]

Zheng C, Bieri KW, Hwaun E, and Colgin LL (2016). Fast gamma rhythms in the hippocampus promote encoding of novel object-place pairings. ENeuro 3, 3089–3096. 10.1523/eneuro.0001-16.2016.

Zhou Y, Lai CSW, Bai Y, Li W, Zhao R, Yang G, Frank MG, and Gan WB (2020). REM sleep promotes experience-dependent dendritic spine elimination in the mouse cortex. Nat. Commun 11, 4819. 10.1038/s41467-020-18592-5. [PubMed: 32968048]

Highlights

- Two distinct interhemispheric communication mechanisms within a single theta cycle
- Splines are 140-Hz rhythms reflecting anti-phase neuronal firing across hemispheres
- Splines are strongest in the granular retrosplenial cortex and seen in rats and mice
- Balance of anti-phase splines and in-phase gamma is dynamically regulated by behavior

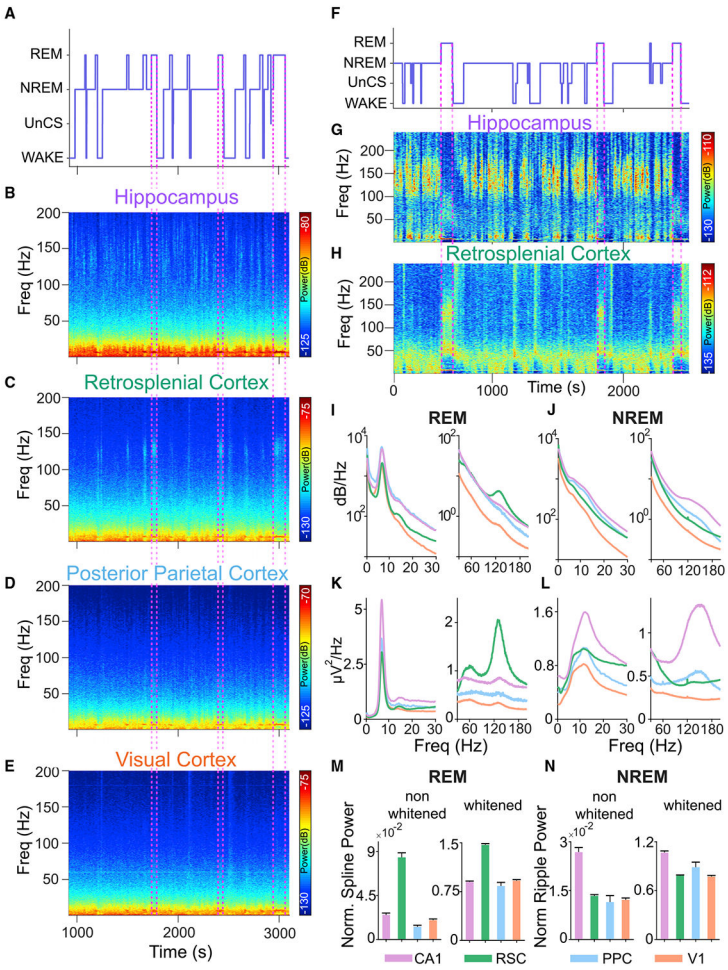

Figure 1. Splines are 110–160 Hz oscillations, strongest in the retrosplenial cortex during REM sleep

(A) Hypnogram from a sleep session with multiple NREM-REM transitions.

(B–E) Corresponding spectrograms from hippocampal CA1, retrosplenial cortex (RSC), posterior parietal cortex (PPC), and primary visual cortex (V1), respectively. While CA1 shows typical NREM ripples (B), another high-frequency oscillation in the 110–160 Hz range, which we refer to as splines, is seen in the RSC (C) during REM sleep. Hippocampal NREM ripples thus alternate with RSC REM splines. Weak ripple and spline power during NREM and REM, respectively, were observed in PPC and V1 (D and E).

(F) Hypnogram from a sleep session in a separate rat.

(G and H) Corresponding whitened spectrograms from CA1 (G) and RSC (H), respectively, showing ripples in CA1 during NREM sleep alternating with splines in RSC during REM sleep.

(I) Averaged spectra during REM sleep across CA1 (purple), RSC (green), PPC (blue), and V1 (orange). The low- (0–30 Hz) and high- (30–200 Hz) frequency bands have been separated for greater clarity. All four regions show high theta power during REM sleep. However, only RSC shows significantly more spline power.

(J) Averaged spectra during NREM across CA1 (purple), RSC (green), PPC (blue), and V1 (orange). CA1 shows high power in the ripple band (110–190 Hz) during NREM sleep. Note the very weak cortical ripples in PPC and RSC.

(K and L) Same as (I and J), but now showing averaged whitened power spectra for REM sleep (K) and NREM sleep (L).

(M) Normalized spline power with pre- and post-whitened values. This ratio is significantly higher during REM sleep in RSC as compared with CA1, PPC, and V1 (rank-sum test, $p < 0.0001$ in all cases).

(N) Normalized ripple power with pre- and post-whitened values. This ratio is significantly higher in CA1 during NREM compared with all other regions (rank-sum test, $p < 0.05$ in all cases).

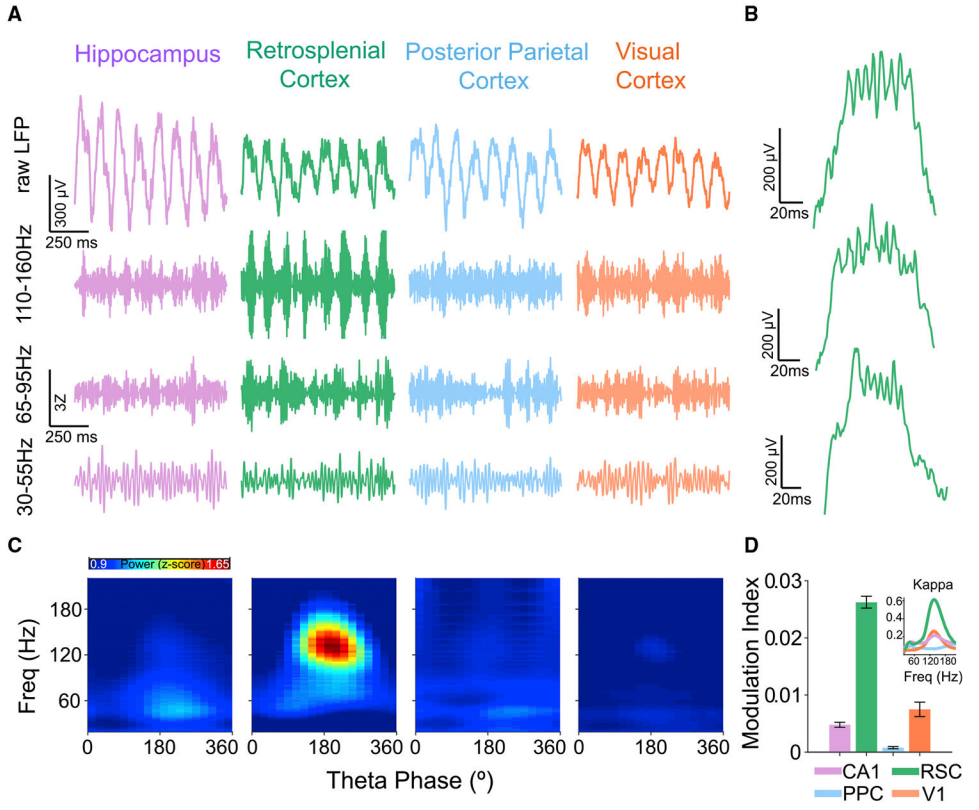

Figure 2. Retrosplenial splines are precisely coupled to the peak of theta

(A) Examples of simultaneously recorded raw and filtered LFP traces during REM sleep from CA1 (purple), RSC (green), PPC (blue), and V1 (orange) showing theta oscillations in all four brain regions with strong spline oscillations (110–160 Hz) at the peak of theta exclusively in RSC. Power in high-gamma (65–95 Hz) and low-gamma (30–55 Hz) bands is much weaker than spline power in RSC and often phase-shifted compared with splines.

(B) Single retrosplenial theta cycle examples during REM sleep from three rats. Splines are consistently locked to the peak of RSC theta in all animals.

(C) Population theta phase-amplitude coupling across the four brain regions during REM sleep. A phase of 180° represents the peak of theta. Splines are precisely coupled to the peak of RSC theta.

(D) Strength of theta phase-amplitude coupling quantified for each LFP using the modulation index (MI) metric. Splines are more precisely coupled to theta in the RSC than in any other brain region (rank-sum test, $p < 0.001$). Inset shows kappa (measure of strength of phase-locking for circular variables) values for theta phase-amplitude coupling of each frequency. Kappa for splines was significantly higher (rank-sum test, $p < 0.0001$) in RSC compared with CA1, PPC, and V1.

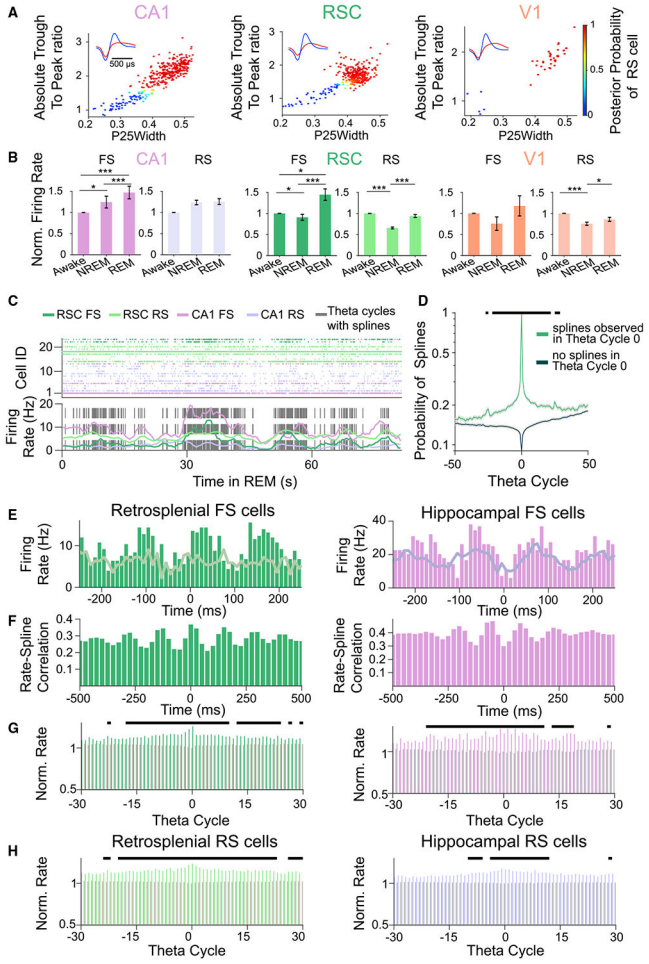

Figure 3. Retrosplenial splines demarcate high-activity REM sleep frames

(A) Features used to classify cells into putative fast-spiking (FS) and regular-spiking (RS) clusters using a Gaussian mixture model. P25Width is the width of the waveform at 25% of the peak amplitude. The color bar shows the posterior probability of a cell being classified as an RS cell. Thus, red dots represent putative RS cells and blue dots represent putative FS cells.

(B) Firing rates (normalized to awake firing rate) of FS and RS cells across CA1, RSC, and V1 across sleep/wake states. RSC FS cells fired at significantly higher rates during REM compared with NREM or awake states.

(C) Raster plot of FS and RS cells from RSC and CA1 during a single REM epoch (top), with average firing rate of each cell type plotted below. Gray dashed lines represent peaks of RSC theta cycles with splines. Theta cycles with splines cluster together into frames and the firing rates of retrosplenial FS and RS cells increase during the spline-rich frames.

(D) Probability of observing RSC theta cycles with splines triggered off theta cycles with (green) or without (black) splines across three rats from which single units were recorded during REM sleep. When theta cycle 0 contains splines, the probability of observing additional theta cycles with splines remains elevated for −22 to +22 theta cycles before and after theta cycle 0 (black bars show theta cycles with effect size ≥0.5).

(E) (Left) Peristimulus time histogram (PSTH) of representative RSC FS cell triggered at the peak of RSC theta cycles with (dark green bars) and without (light green line plot) splines. Spline-triggered averages show sustained increases in both the rate and theta modulation of FS firing. (Right) Similar plot, now shown for a CA1 FS cell firing, again triggered at the peak of RSC theta cycles with (purple bars) and without (gray line plot) splines. The CA1 FS cell also shows sustained increases in firing rate around splines.

(F) Correlation between firing rate and RSC spline power for the same RSC and CA1 FS cells shown in (E).

(G) Normalized firing rate of FS cells for RSC (left) and CA1 (right) across ±30 theta cycles centered on theta cycles with (green bars for RSC; purple for CA1) and without (gray bars) RSC splines. The cycles where the effect size was ≥0.5 are marked by black bars. FS cells in both RSC and CA1 showed sustained increases in firing rates during the high-activity REM frames demarcated by RSC splines.

(H) Same as (G) but for RS cells. RS cells in both RSC and CA1 showed sustained increases in firing rates during the high-activity REM frames demarcated by RSC splines.

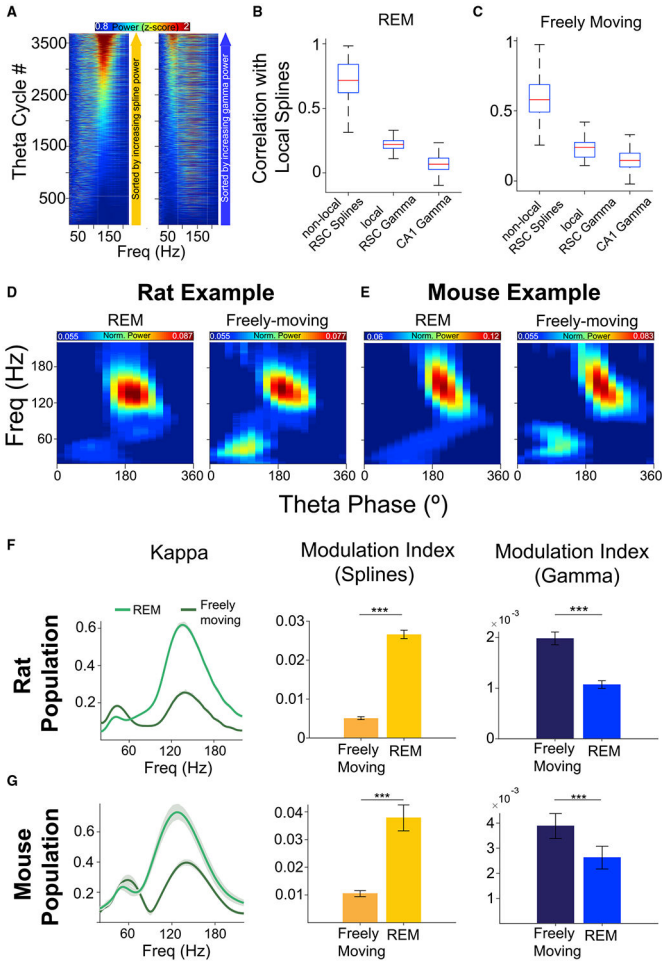

Figure 4. Splines and gamma are independent and differentially expressed during REM sleep versus freely moving states in both rats and mice

(A) All theta cycles during an example REM epoch sorted by either spline (110–160 Hz; left) or gamma (30–80 Hz; right) power showing the independence of splines and gamma.

(B) Population correlation coefficients of RSC splines with: (left) RSC splines at separate ("non-local") simultaneously recorded RSC locations spanning a distance of 0.06–2.5 mm from the local electrode; (middle) RSC gamma on the same local electrode; (right) CA1 gamma on CA1 electrodes at a distance of 1.5–2.8 mm from the RSC local electrode) during REM. Spline power across distant RSC electrodes is strongly correlated and is significantly higher than correlations with local RSC gamma (rank-sum test, $p < 0.001$) and CA1 gamma (rank-sum test, $p < 0.001$). Thus, splines occur independently of RSC gamma and CA1 gamma but are strongly correlated across the long axis of the RSC.

(C) Same as (B) but for freely moving behavior (speed >5 cm/s). Spline power across distant RSC locations was strongly correlated and was significantly higher than correlations with local RSC gamma (rank-sum test, $p < 0.001$) and CA1 gamma (rank-sum test, $p < 0.001$) during awake active states.

(D) Example RSC theta phase-amplitude coupling showing stronger gamma in freely moving behavior than REM sleep in rats.

(E) Same as (D), but from a mouse session.

(F) The balance of theta-coupled splines and gamma is dynamically regulated by behavior in rats. Kappa and modulation index are two measures quantifying the strength of theta-coupling. Splines are dominant during REM sleep, but theta-coupled splines decrease and gamma increases during freely moving behavior.
(G) Same as (F) but for mice, showing that the balance of splines and gamma is similarly controlled by behavior in both rats and mice.

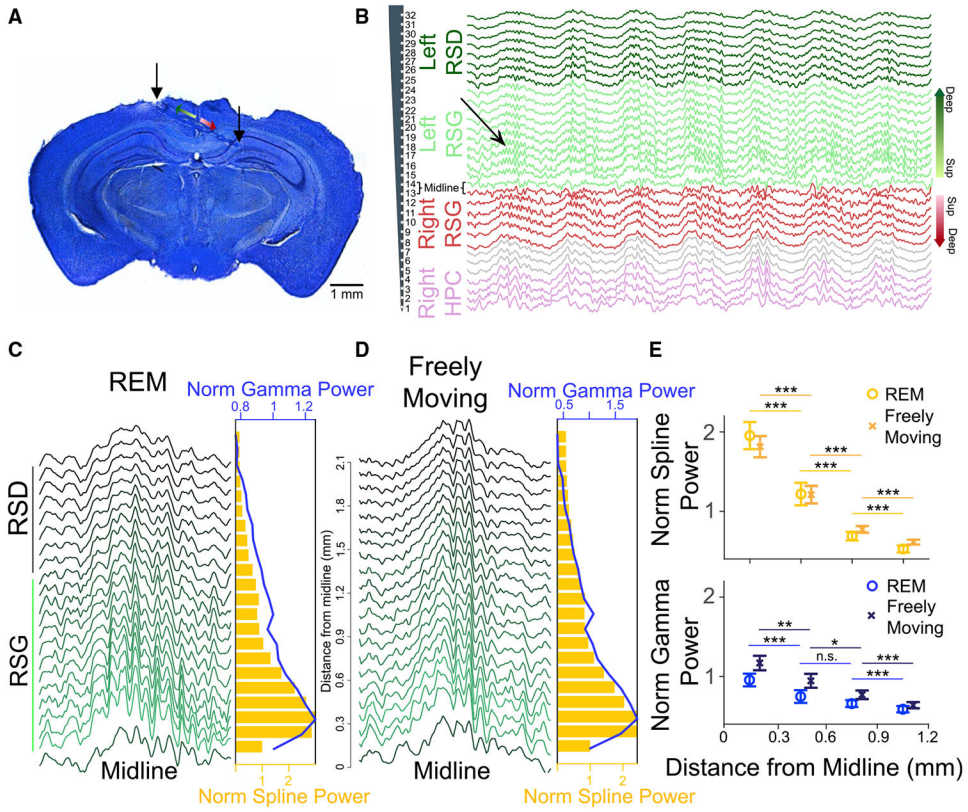

Figure 5. Splines are strongest in the superficial layers of the retrosplenial cortex during REM and awake active states

(A) Histology showing laminar probe implanted bilaterally in the RSC, allowing simultaneous recordings from multiple layers across both hemispheres. Superficial (lighter colors) and deep (darker colors) layers in left (green) and right (red) RSG hemispheres are highlighted.

(B) Raw LFP recorded from a 32-channel probe shows splines are strongest in the superficial layers of the RSC. The probe spanned left RSD (dark green), left RSG (light green), and crossed the midline into right RSG (red) and CA1 (purple). Gray traces show channels in white matter. Channels in superficial (Sup) and deep layers have been highlighted and correspond to the schematic in (A).

(C) Left: Example theta cycle across channels from the left hemisphere during REM sleep (bottom trace is the midline/layer 1 channel closest to the first contact in left RSG). Right: Spline power (gold bars) and gamma power (blue line) across channels during the REM session show splines and gamma oscillations are strongest in the superficial layers.

(D) Similar to (C), but for freely moving behavior (speed >5 cm/s). Splines and gamma are again strongest in the superficial layers of RSC.

(E) Normalized spline power and gamma power across three mice (nine sessions each from REM and awake). The mean spline and gamma power during REM and awake states was significantly higher in the superficial layers and decreased with distance from midline.

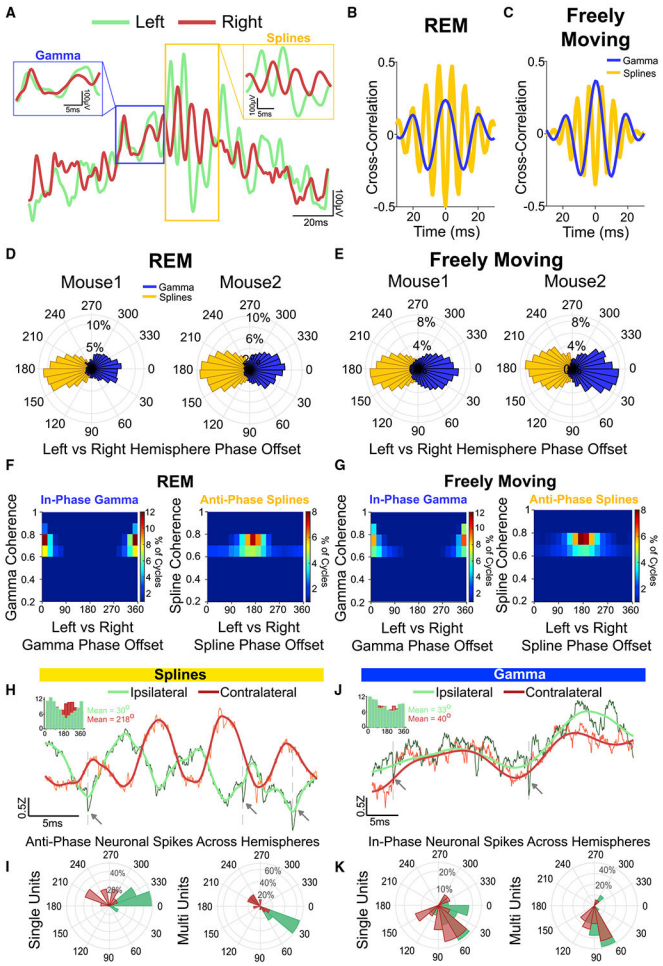

Figure 6. Splines are anti-phase across hemispheres while gamma oscillations are in-phase during REM sleep and awake active states

(A) Example raw LFP trace during REM showing a theta cycle from the left hemisphere (green) overlaid with a simultaneously recorded LFP from the right hemisphere (red). Gamma oscillations were in phase, but splines in the contralateral hemisphere were 180° out of phase (insets show zoomed views).

(B) Cross-correlation from a REM session shows that splines (gold) were anti-phase across hemispheres while gamma oscillations (blue) were in-phase.

(C) Same as (B) during a freely moving session.

(D) Distribution of coherence phase (degrees) between the left and right hemisphere during REM sessions from two mice. A clear 180-degree phase offset was seen for splines.

(E) Same as (D) during freely moving sessions.

(F) Distribution of spline and gamma coherence magnitude and phase (degrees) across three mice (nine sessions) shows that splines were consistently anti-phase (mean phase = 163°, kappa = 0.7) across hemispheres while gamma oscillations were in-phase (mean phase = 2°, kappa = 2.2) during REM.

(G) Same as (F) during freely moving sessions (three mice, nine sessions) shows that splines were consistently anti-phase across hemispheres (mean phase = 180°, kappa = 0.9) while gamma oscillations were in-phase (mean phase = 2.2°, kappa = 1.6).

(H) Example raw (black) and 3–500 Hz filtered (green) LFP showing spikes (dotted lines, arrows) at the trough of local splines. A simultaneously recorded raw (orange) and 3–500 Hz filtered (red) LFP from the contralateral hemisphere shows the same spikes locked to the peak of contralateral splines. Inset shows phase-locking from a single unit to local (green) and contralateral (red) splines showing significant phase-locking to the trough of ipsilateral (local) splines (mean phase = 30°, ln(Rayleigh's Z) = 3.9, $p < 0.001$) and the peak of contralateral splines (mean phase = 218°, ln(Rayleigh's Z) = 2.4, $p < 0.001$).
(I) Mean phase distribution (degrees) of the significantly phase-locked cells to local and contralateral splines. There was a significant difference between the preferred phase for ipsilateral compared with contralateral splines (Watson Williams test, $p < 0.0001$).
(J) Example raw (black) and 3–80 Hz filtered (green) LFP showing spikes (dotted lines, arrows) at the trough of gamma. A simultaneously recorded raw (orange) and 3–80 Hz filtered (red) LFP from a contralateral channel shows the same spikes locked to the trough of gamma. Inset shows phase-locking from a single unit to local (green) and contralateral (red) gamma showing significant phase-locking to the trough of both ipsilateral (local) gamma (mean phase = 33°, ln(Rayleigh's Z) = 3.42, $p < 0.001$) and contralateral gamma (mean phase = 40°, ln(Rayleigh's Z) = 2.2, $p < 0.001$).
(K) Mean gamma phase distribution (degrees) of the significantly phase-locked cells. There was no significant difference between the preferred phase distributions for ipsilateral versus contralateral gamma rhythms (Watson Williams test, $p = 0.16$).

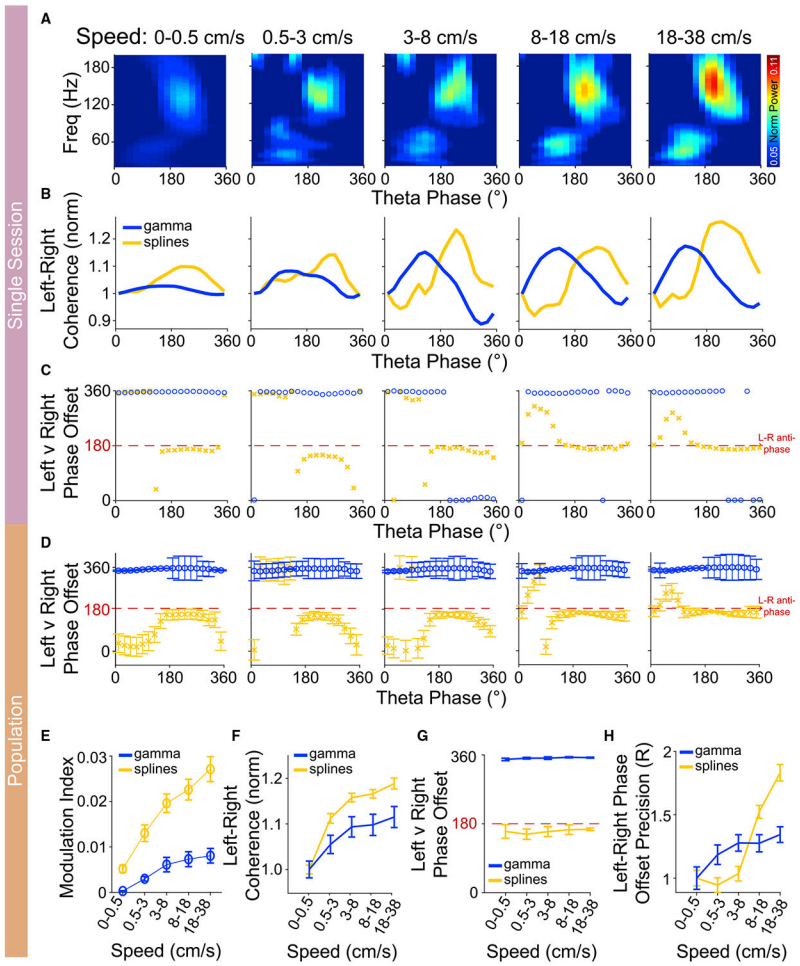

Figure 7. Spline and gamma interhemispheric coherence increase at faster running speeds

(A) Example phase-amplitude coupling at increasing running speeds. Theta-coupling of splines increased at faster running speeds as head-fixed mice ran on a spherical ball.

(B) Spline and gamma coherence magnitude as a function of theta phase at increasing running speed from an example session. Note that spline coherence was maximum at the peak of theta corresponding to the maximum spline power within a theta cycle, as seen in (A) above. Similarly, gamma coherence peaked during the rising phase of theta.

(C) Spline and gamma coherence phase as a function of theta phase with increasing running speed from the same session as (B). Splines were anti-phase specifically at the peak of theta when their power and coherence were the highest.

(D) Spline and gamma coherence phase offset as a function of theta phase across the population (three mice, nine sessions). Splines were consistently anti-phase at the peak of theta.

(E) There was a significant effect of speed on the modulation index of both splines and gamma ($p < 0.001$). However, the effect size at fast versus slow speeds was higher for splines ($d = 2.1$) compared with gamma ($d = 1.4$).

(F) Spline and gamma coherence magnitude increased with running speed. There was a significant effect of speed on the magnitude of spline ($p < 0.001$) and gamma coherence ($p <$

0.001). The effect size for the increase in coherence at fast versus slow speeds was stronger for splines (d = 1.2) compared with gamma (d = 0.6).

(G) Splines were anti-phase, and gamma oscillations were in-phase with increasing running speed. Note, however, that the variance in the phase-offset decreased with increasing running speed.

(H) The left-right phase offset precision increased with increasing running speed. The effect size at fast versus slow speeds was stronger for splines (d = 1.4) as compared with gamma (d = 0.4).

KEY RESOURCES TABLE

REAGENT or RESOURCE	SOURCE	IDENTIFIER
Experimental models: Organisms/strains		
Rat: Long Evans	Charles River Laboratories	Crl: LE 006
Rat: Sprague-Dawley	Charles River Laboratories	Crl: SD 400
Mouse: C57BL/6	The Jackson Laboratory	JAX: 000664
Software and algorithms		
MATLAB	Mathworks	RRID: SCR_001622
Cheetah acquisition software	Neuralynx	https://neuralynx.com/
OpenEphys acquisition system	Siegle et al. (2017)	https://open-ephys.org/
DeepLabCut	Mathis et al. (2018)	https://github.com/DeepLabCut
Offline Sorter	Plexon Inc	https://plexon.com/products/offline-sorter/